Journal of Nuclear Materials 384 (2009) 195–211

Contents lists available at ScienceDirect

Journal of Nuclear Materials

journal homepage: www.elsevier.com/locate/jnucmat

The effect of neutron irradiation on the fiber/matrix interphase of silicon carbide composites

T. Nozawa *, Y. Katoh, L.L. Snead

Materials Science and Technology Division, Oak Ridge National Laboratory, P.O. Box 2008, Oak Ridge, TN 37831-6138, USA

ARTICLE INFO

Article history:
Received 11 July 2008
Accepted 13 November 2008

ABSTRACT

Given the good stability of mechanical properties of silicon carbide (SiC) under neutron irradiation, the ultimate irradiation tolerance of SiC composite materials may be limited by the fiber/matrix interphase, which is critically important to the performance of these composites. This study investigates the irradiation stability of pyrolytic carbon (PyC) monolayer and PyC/SiC multilayer interphases by tensile and single fiber push-out test techniques. Neutron irradiation was performed to doses of 0.7–7.7 dpa at temperatures from 380 to 1080 °C. Both interfacial debond shear strength and interfacial friction stress apparently decrease by irradiation, although this is not so dramatic when $T_{irr} < 1000$ °C. In contrast, the interfacial shear stresses are most affected by the higher temperature irradiation (>1000 °C). Noteworthy, these irradiation effects depend on the type of interphase material, i.e., for the pyrolytic carbon or multilayer SiC variants studied. In the range of irradiation temperature and dose, the degradation in interfacial shear properties, while measurable, is not of a magnitude to degrade the mechanical performance of the composites. This was observed for both interphase types studied. In particular, the proportional limit tensile stress decreases slightly by irradiation while the tensile fracture strength undergoes very minor change.

1. Introduction

Silicon carbide (SiC) has been widely used for high-temperature engineering applications due to its inherently high thermo-chemical stability, good oxidation resistance, and strength retention at high-temperatures. Moreover, its resistance to neutron irradiation, e.g., low-induced radioactivity and low irradiation-induced after-heat, gives scope for a potential application in fusion and advanced nuclear fission energy systems [1]. Additionally, it has been proven that SiC in a stoichiometric form offers exceptional retention of mechanical properties under neutron irradiation. High-purity chemical-vapor-deposited (CVD) SiC reportedly retains its strength by neutron irradiation at least to ~20 dpa [2–4].

Due to inherent brittleness of SiC in its monolithic form, SiC is being developed for use in the composite form, combining a SiC fiber, a SiC matrix, and a fiber/matrix (F/M) interphase. Near-stoichiometric and highly-crystalline SiC, e.g., Hi-Nicalon™ Type-S or Tyranno™-SA SiC fibers, and a chemical-vapor-infiltrated (CVI) SiC matrix, are generally adopted because of their better irradiation tolerance. A poorly graphitized pyrolytic carbon (PyC) is typically adopted as an F/M interphase, which serves to intercept and tie-up propagating cracks. Since the enhanced fracture toughness and ultimate performance of composites is critically dependent on this interphase, its irradiation stability, and the combined effects of environment and irradiation on the fiber, matrix, and interphase is of critical importance.

The effect of neutron irradiation on the F/M interface was first evaluated on Nicalon™/CVI-SiC composites with PyC as an F/M interphase [5,6]. In this composite system, the crystalline CVI-SiC matrix swells by irradiation depending on irradiation temperature and neutron dose, typical of ceramic materials. However, the poorly-crystallized glassy Nicalon™ fiber underwent densification. Due to this differential irradiation-induced dimensional change between Nicalon™ and CVI-SiC, comparably large stresses generate at the F/M interface, resulting in shear failure of the composites, i.e., shape instability probably induced by strong contribution of trans-interface tensile stress [5]. Meanwhile, this shape instability issue has been solved by adopting near-stoichiometric and highly-crystalline advanced third generation SiC fibers such as Hi-Nicalon™ Type-S and Tyranno™-SA. Since both advanced SiC fibers and CVI-SiC matrix swell in similar manners, irradiation-induced shear stresses at the F/M interface are minimized. Indeed, no major macroscopic deformation by irradiation has been identified for Hi-Nicalon™ Type-S/CVI-SiC composite system [7]. Moreover, no significant deterioration of flexural and tensile properties has been reported [8–10].

---

* Corresponding author. Present address: Fusion Research and Development Directorate, Japan Atomic Energy Agency, 2-4 Shirakata Shirane, Tokai, Ibaraki 319-1195, Japan. Tel.: +81 29 282 6416; fax: +81 29 284 3589.
E-mail address: nozawa.takashi67@jaea.go.jp (T. Nozawa).

0022-3115/$ - see front matter © 2008 Elsevier B.V. All rights reserved.
doi:10.1016/j.jnucmat.2008.11.015

Hinoki et al. [11] closely investigated the irradiation effect on the interfacial shear properties by the push-in technique and compared the influence on varied interphases: a PyC monolayer, a PyC/SiC multilayer, and a pseudo 'porous' SiC interphase. By neutron irradiation up to 0.5 dpa at 300–500 °C, slight deformation for any interphase studies was observed. A decrease of interfacial shear properties was also identified by the double notch shear test method for irradiation up to 1 dpa at 800–1000 °C for the same series of composites [12]. In both cases, SiC/SiC composites with pseudo-porous SiC interphase severely deteriorated their interfacial properties. In recent work by the authors [13], interfacial shear properties for Hi-Nicalon™ Type-S/CVI-SiC composites with either a PyC monolayer or a PyC/SiC multilayer interphase were investigated for the limited irradiation condition ($\phi = 7.7$ dpa, $T_{irr} = 800$ °C). The results indicate (1) a very minor irradiation effect on interfacial shear properties for the monolayer composites and (2) a slight irradiation-induced decrease of shear stresses for the multilayer composites. This difference is somewhat surprising since it has been believed that the thinly-layered carbon interphases would be more radiation-stable.

Table 1
Key characteristics of unidirectional Hi-Nicalon™ Type-S/CVI-SiC composites.

Interphase	Fiber volume fraction	Porosity	Density (g/cm^3)
PyC	~0.29	~0.15	~2.57
Multilayer	~0.38	~0.14	~2.66

While there is a growing body of work evaluating the F/M interphase, fundamental knowledge about the irradiation effect on the F/M interphase is still insufficient. Specifically, a fundamental question about the irradiation tolerance of the multilayer interphase is unanswered. The goal of the following study is to provide data and analysis of the effect of neutron irradiation on the F/M interphase to help bridge this knowledge gap.

2. Experimental

2.1. Materials

Materials evaluated were unidirectional SiC/SiC composites (Hyper-Therm High-Temperature Composites Inc., Huntington Beach, CA) with varied F/M interphases (Table 1). Reinforcing SiC fibers were Hi-Nicalon™ Type-S (3.1 g/cm^3, Si/C = 1.05). A high-purity and high-crystallinity SiC matrix was chemical-vapor-infiltrated. A PyC monolayer or a PyC/SiC multilayer interphase was chemically deposited on the fiber surface in advance of matrix densification. Thickness of the PyC monolayer was 520–720 nm. In contrast, the multilayer interphase was composed of a sequence of ~20 nm-thick PyC and ~100 nm-thick SiC sub-layers (Fig. 1). The fiber volume fraction and porosity were 30–40% and 15–20%, respectively. The high-porosity of these CVI-SiC/SiC composites was due primarily to the presence of columnar pores along the fiber bundles. Key characteristics of these composites have been reported elsewhere [12–14].

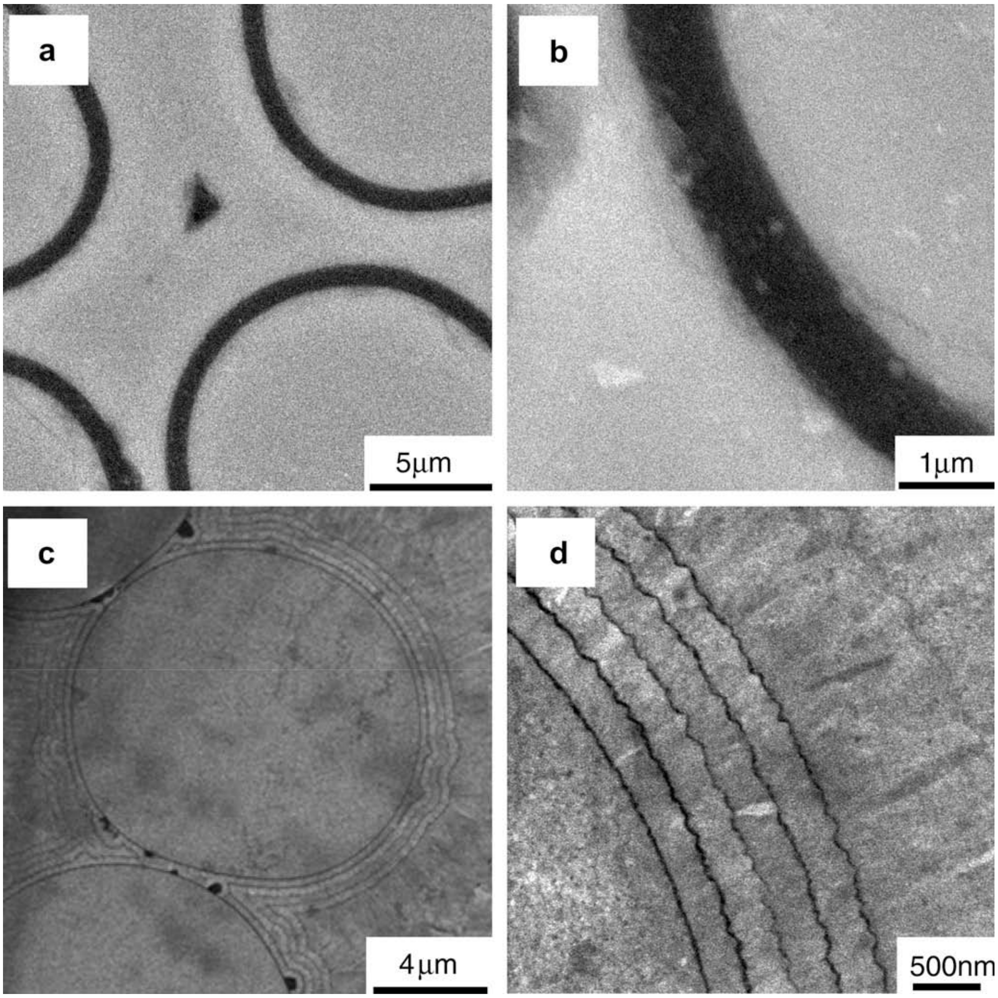

Fig. 1. Typical microstructural images of (a), (b) PyC monolayer and (c), (d) PyC/SiC multilayer interphases of as-received SiC/SiC composites [13].

2.2. Neutron irradiation

Two types of neutron irradiation campaigns were performed in the High Flux Isotope Reactor (HFIR) at Oak Ridge National Laboratory. The HFIR-14 J fixed-core capsule irradiation was performed in an unshielded removable beryllium position of the HFIR. Irradiation dose was 7.7 dpa assuming 1.0×10^{25} n/m^2 (E > 0.1 MeV) corresponds to one displacement per atom (1 dpa), while the irradiation temperature was ~800 °C. In contrast, small-capsule rabbit irradiations were performed in the hydraulic tube of the HFIR under the FUN and NERI SiC/SiC series of irradiations. The neutron doses were 0.7–4.2 dpa and irradiation temperatures were in the range of 380–1080 °C. Irradiation temperature was measured and controlled in-situ by thermocouples and capsule sweep–gas mixtures for the HFIR-14 experiment. The uncertainty of irradiation temperatures was reasonably low (±20 °C). In contrast, irradiation temperatures in rabbit irradiation were estimated by the isochronal annealing of CVD-SiC temperature monitors. In principle, the temperature monitor gives the temperature near the end of the irradiation period with a similar uncertainty to the instrument experiment (±20 °C) [15,16].

2.3. Tensile test

Following a guideline of ASTM C1275-00, cyclic unloading/reloading tensile tests were conducted at ambient-temperature using an electromechanical testing machine. Rectangular miniature tensile specimens with a gauge size of either $20^{\mathrm{L}} \times 4^{\mathrm{W}} \times 1.5^{\mathrm{T}}$ or $20^{\mathrm{L}} \times 2^{\mathrm{W}} \times 1.5^{\mathrm{T}}$ mm^3 were prepared. Note that the total specimen length of 50 mm was fixed for all specimens. Specimen size effect is a potential concern when testing these specimens. Considering the structural minimum unit width (or thickness) of the unidirectional composites is larger than the width (or thickness) of the mono fiber bundle (<1 mm), a very minor effect of specimen size on tensile properties, which depend on the axial fiber volume fraction, is expected in the size range of concern [17]. Indeed, no significant size effect was found in this study. The tensile specimen was passively gripped via aluminum grip-end tabs using a pneumatic wedge-type gripping device. Tensile strain was measured by a pair of strain gauges with a gauge length of 5.0 mm, which were adhesively bonded on specimen surfaces of the middle gauge section. A constant crosshead displacement rate was 0.5 mm/min.

Young's modulus was defined as an initial tangent modulus in the tensile stress–strain curve. Proportional limit tensile stress (PLS) was determined as a stress of 5% deviation in stress from initial linearity following ASTM C1275-00. Ultimate tensile strength (UTS) and total elongation were defined as a stress and a strain at composite fracture, respectively.

2.4. Single fiber push-out test

Single fiber push-out tests were conducted at room-temperature using a nano-indentation test system. A thin-strip specimen with a thickness of 30–220 μm was cut from the tensile specimen with both surfaces polished by the standard metallographic techniques to a surface finish of ~0.5 μm. The specimen was bonded on the specimen holder above a narrow groove. The fiber was then randomly selected and monotonically loaded up to the maximum system allowable load capacity (650 mN). A Berkovich indenter tip was used in this experiment. An applied load rate was 0.05 N/N · s. Details of the fiber push-out test technique have been described elsewhere [18]. Microstructures of the F/M interphase and the pushed-out fiber surface were observed by scanning electron microscopy (SEM) for both as-received and neutron irradiated materials.

Of many stress parameters, two interfacial shear properties: (1) an interfacial debond shear strength (τ_s) as a critical shear stress to induce an interfacial crack along the bonded F/M interface, and (2) an interfacial friction stress (τ_f) at the debonded interface are defined. Both τ_s and τ_f are calculated using experimental push-out test results of (1) a debond initiation stress (σ_d) and (2) a complete debonding and sliding stress ($\sigma_{\max}$) as defined in Fig. 2. In the following discussion, a compressive stress is denoted with a negative sign. For evaluation of this type of data, various analytical models have been developed [18–24]. Of these models, a non-linear shear-lag model proposed by Hsueh [21] becomes a basis to evaluate τ_s considering the precise stress interaction at the F/M interface: (1) the radial dependence of the axial stresses in both the fiber and the matrix, (2) the shear stress distribution in the matrix and (3) the exact equilibrium equation in relating the tangential stress to the radial stress at the interface. Hsueh further developed a double shear-lag model by separately considering the stress interactions among the fiber, matrix and F/M interphase [22]. One major drawback of the original Hsueh models is limited applicability to isotropic constituents. In the modified double shear-lag model by the authors (see Appendix), anisotropy of the constituents is considered. Besides, residual stresses induced by thermal expansion mismatch and by differential swelling among the fiber, F/M interphase, and matrix can be discussed together in the model, although the effect of dynamic phenomena such as irradiation creep of SiC and PyC was ignored for simplicity. In contrast, Shetty [24] originally discussed the interfacial friction issue for the debonded interface. In the previous work by the authors [25], Shetty's model was updated for anisotropic composites and this method was applied in this study.

The detailed analogy of the modified Hsueh model was discussed elsewhere [22,25]. The resultant form can provide an interfacial debond shear strength (τ_s) as

$$\tau_s = -\frac{r_f \lambda}{2}\left\{\frac{\sigma_d[\exp(\lambda t)+\exp(-\lambda t)] - Z(\sigma_d+\sigma_{th}+\sigma_{irr})[\exp(\lambda t)+\exp(-\lambda t)-2]}{\exp(\lambda t)-\exp(-\lambda t)}\right\}, \tag{1}$$

where the constants λ and Z are determined by dimensions and elastic constants of the constituents, and σ_{th} and σ_{irr} are stress parameters defined by the thermal expansion mismatch and the differential swelling among the fiber, matrix and F/M interphase, respectively (see Appendix). Assuming no contribution from the thermal residual stress (or irradiation-induced stress), σ_{th} (or σ_{irr}) becomes zero.

Assuming a coulomb friction, an interfacial friction stress (τ_f) can be determined as [25]:

$$\tau_f = -\mu(\sigma_r^{th} + \sigma_r^{rough} + \sigma_r^{irrad}), \tag{2}$$

where, μ is a coefficient of friction and σ_r^{th}, σ_r^{rough} and σ_r^{irrad} are radial clamping stresses induced by thermal expansion mismatch, fiber surface roughness and differential swelling, respectively. These

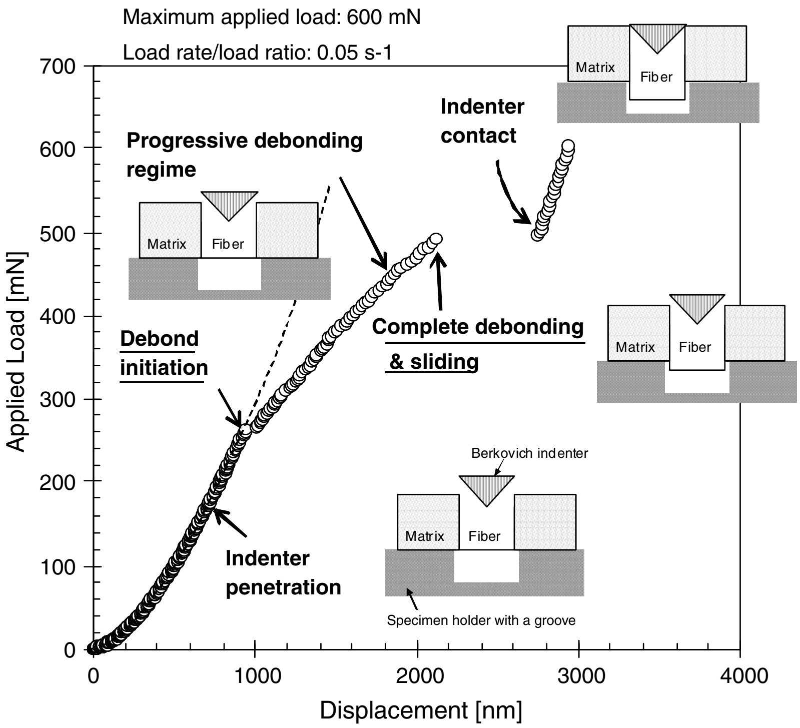

Fig. 2. Schematic of the load-displacement curve of the fiber push-out test. Two experimental parameters: (1) a debond initiation load (σ_d) and (2) a complete debonding and sliding load ($\sigma_{\max}$) are defined.

clamping stresses have a close relationship with a measured sliding stress ($\sigma_{\max}$) as

$$\sigma_{\max} = -\frac{E_f(1+\nu_c)}{E_c\nu_f}\left(\sigma_r^{\text{th}} + \sigma_r^{\text{rough}} + \sigma_r^{\text{irrad}}\right)\left[\exp\left(\frac{2\mu E_c \nu_f t}{r_f E_f(1+\nu_c)}\right) - 1\right], \tag{3}$$

where E and ν are Young's modulus and Poisson's ratio. Subscripts f and c denote the fiber and the composites, respectively. Note that the modified Shetty's model assumes a fiber surrounded by a composite average, i.e., the two-phase cylindrical system, since there is no clear solution for multi-phase system so far. When specimens are sufficiently thin, τ_f consequently becomes proportional to $\sigma_{\max}/t$ regardless of material properties of the constituents,

$$\tau_f \cong -\frac{r_f}{2}\cdot\frac{\sigma_{\max}}{t}. \tag{4}$$

2.5. Materials properties for calculation

The input values used in calculation are empirically obtained [2,4,26–38] and are summarized in Table 2. According to the study by Yan et al. [39], PyC as an F/M interphase is more graphitic near the fibers (6–10 nm), while the structure becomes more turbostratic along the radial direction, i.e., near-isotropic. It is noteworthy that the structure of PyC depends significantly on processing conditions. Because of this structural uncertainty for PyC, this study considers two types of turbostratic carbon: a high-density carbon [26] and a low-density carbon [35]. A major difference between the high-density PyC and low-density PyC is in thermal expansivity as well as density and this issue is discussed later. The actual structure of PyC applied in this study should be classified between these two materials.

A high-density (~2 g/cm^3) turbostratic carbon with Bacon anisotropy factor of ~1 is assumed for PyC interphase. The coefficient of thermal expansion (CTE) is assumed to be 5.5 × 10^{-6}/°C. From many irradiation studies, the high-density isotropic carbon undergoes shrinkage first and swells with increasing neutron fluence in the direction perpendicular to the deposition plane, while it shrinks monotonically in the direction parallel to the deposition plane [26]. An empirical fit of the swelling was provided in [27].

Table 2
List of material properties applied in the analytical model.

Valuables	Non-irradiated	Irradiated
High-density isotropic carbon [26]		
Density (g/cm^3)	$d_0 = 1.9$	$=d_0(1+3\varepsilon)$
Elastic modulus (GPa)	$E_0 = 25$	$=E_0(1+0.23\phi)$
Poisson's ratio	$\nu_0 = 0.2$	Assuming no change
CTE (10^{-6}/°C)	$\alpha_0 = 5.5$	Assuming no change
Linear swelling	–	Fig. 3 in Ref. [26]
Low-density isotropic carbon (glassy carbon) [35]		
Density (g/cm^3)	$d_0 = 1.5$	$=d_0(1+3\varepsilon)$
Elastic modulus (GPa)	$E_0 = 25$	Fig. 4 in Ref. [35]
Poisson's ratio	$\nu_0 = 0.2$ (assumed)	Assuming no change
CTE(10^{-6}/°C)	$\alpha_0 = 2.8$	Assuming no change
Linear swelling	–	Fig. 1 in Ref. [35]
CVD-SiC [4]		
Density (g/cm^3)	$d_0 = 3.2$	$=d_0(1+3\varepsilon)$
Elastic modulus (GPa)	$E_0 = 460$	$=E_0(1-.9\varepsilon)$ when $T_{\text{irr}} < 1000$ °C Assuming no change when $T_{\text{irr}} > 1000$ °C
Poisson's ratio	$\nu_0 = 0.2$	Assuming no change
CTE(10^{-6}/°C)	$\alpha_0 = 4.4$	Assuming no change
Linear swelling	–	Fig. 22 in Ref. [4]
Hi-NicalonType-S [38]		
Density (g/cm^3)	$d_0 = 3.1$	$=d_0(1+3\varepsilon)$
Elastic modulus (GPa)	$E_0 = 420$	$=E_0(1-20.9\varepsilon)$ when $T_{\text{irr}} < 1000$ °C
Poisson's ratio	$\nu_0 = 0.2$	Assuming no change
CTE(10^{-6}/°C)	$\alpha_0 = 5.1$	Assuming no change
Linear swelling	–	Assuming same with CVD-SiC

Linear swelling (ε).
Neutron fluence (ϕ) in units of 10^{25} n/m^2.

Material properties of low-density turbostratic carbon were summarized by Virgil'ev and Lebedev [35]. The density is ~1.5 g/cm^3. The elastic modulus ranged from 25 to 30 GPa. The coefficient of thermal expansion of the low-density carbon is about 2.8×10^{-6}/°C. Neutron irradiation causes a significant shrinkage when T_{irr} = 140–750 °C, resulting in densification. With formation of a new system of micropores, the thermal expansivity of low-density carbon reportedly decreases by irradiation. Because of limited irradiation data available, this study assumes no change of thermal expansivity by irradiation. The elastic modulus of low-density carbon first decreases by irradiation and gradually increases with increasing neutron fluence up to 1×10^{21} n/cm^3. Beyond this fluence, the elastic modulus seems to be saturated (~15% increase of the non-irradiated value).

High-crystallinity and high-purity SiC swells by irradiation with the accumulation of radiation-induced defects and the magnitude of swelling saturates with increasing neutron dose (>1 dpa). For irradiation temperatures less than 1000 °C, swelling is a strong function of temperature, decreasing with increasing temperature. [4]. The irradiation-induced change of Young's modulus of SiC can be well-described by the Tersoff potential and the resulting irradiation effects are well documented [4,40]. Because of lack of irradiation data on advanced SiC fibers, the post-irradiation properties of Hi-Nicalon™ Type-S fiber are presently assumed to be equivalent to those of CVD-SiC. However it is worth noting that recent data [41] identified some discrepancies in post-irradiation properties of SiC fibers with CVD-SiC. The Poisson's ratio and the thermal expansivity of SiC are assumed to be unchanged by irradiation.

Material properties of composites can be estimated by the rule of mixtures, which is modified by Hashin for the transversely isotropic system [42]. In this calculation for multilayer composites,

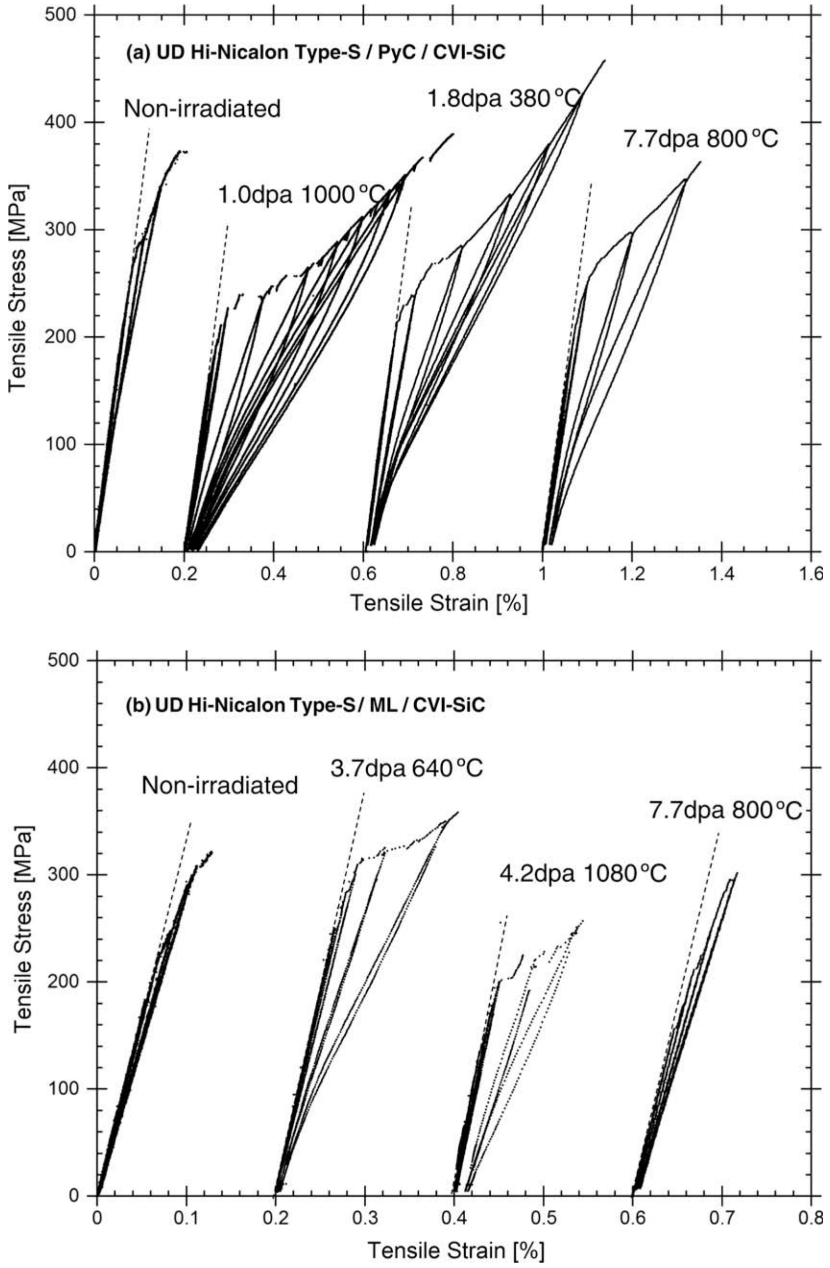

Fig. 3. Typical tensile stress–strain curves of as-received and neutron-irradiated unidirectional Hi-Nicalon™ Type-S/CVI-SiC composites with either (a) a PyC monolayer or (b) a PyC/SiC multilayer interphase.

Table 3
Tensile properties of as-received and irradiated SiC/SiC composites.

Interphase	Irradiation campaign	Irradiation condition	Young's modulus		Ultimate tensile strength		Proportional limit tensile stress		Failure strain		# of valid tests
			E (GPa)	ΔE (%)	σ_{UTS} (MPa)	$\Delta\sigma_{UTS}$ (%)	σ_{PLS} (MPa)	$\Delta\sigma_{PLS}$	ε_{total} (%)	$\Delta\varepsilon_{total}$ (%)	
Monolayer	None	–	362 (34)	–	319 (64)	–	228 (44)	–	0.16 (0.06)	–	25
	JMTR00M-95U	1.0 dpa 800 °C	320 (46)	−12	366 (46)	+15	197 (35)	−14	0.41 (0.17)	+156	8
	JMTR00M-95U	1.0 dpa 1000 °C	289 (16)	−20	418 (24)	+31	183 (45)	−20	No data	No data	6
	HFIR-FUN	1.8 dpa 380 °C	354 (28)	−2	366 (82)	+15	190(23)	−17	0.40 (0.14)	+150	3
	HFIR-14 J	7.7 dpa 800 °C	320 (11)	−12	381 (26)	+19	217 (36)	−5	0.38 (0.02)	+138	4
Multilayer	None	–	375 (19)	–	271 (51)	–	232 (47)	–	0.09 (0.03)	–	14
	HFIR-NERI	0.7 dpa 700 °C	406 (36)	+8	234 (12)	−14	203 (32)	−12	0.06 (0.01)	−33	2
	HFIR-NERI	0.7 dpa 1030 °C	421 (53)	+12	193 (61)	−29	193 (61)	−17	0.04 (0.02)	−56	3
	HFIR-NERI	3.7 dpa 640 °C	366 (52)	−2	296 (57)	+9	211 (53)	−9	0.13 (0.07)	+44	3
	HFIR-NERI	4.2 dpa 1080 °C	433 (54)	+15	257 (–)	−5	136 (–)	−41	0.14 (–)	+56	3
	JMTR00M-95U	1.0 dpa 800 °C	355 (65)	−5	319 (51)	+18	223 (36)	−4	0.15 (0.07)	+67	4
	JMTR00M-95U	1.0 dpa 1000 °C	338 (41)	−10	231 (51)	−15	166 (35)	−28	No data	No data	3
	HFIR-14J	7.7 dpa 800 °C	356 (39)	−5	302 (–)	+11	186 (42)	−20	0.12 (–)	+33	4

Note: Numbers in parenthesis indicate one standard deviation.

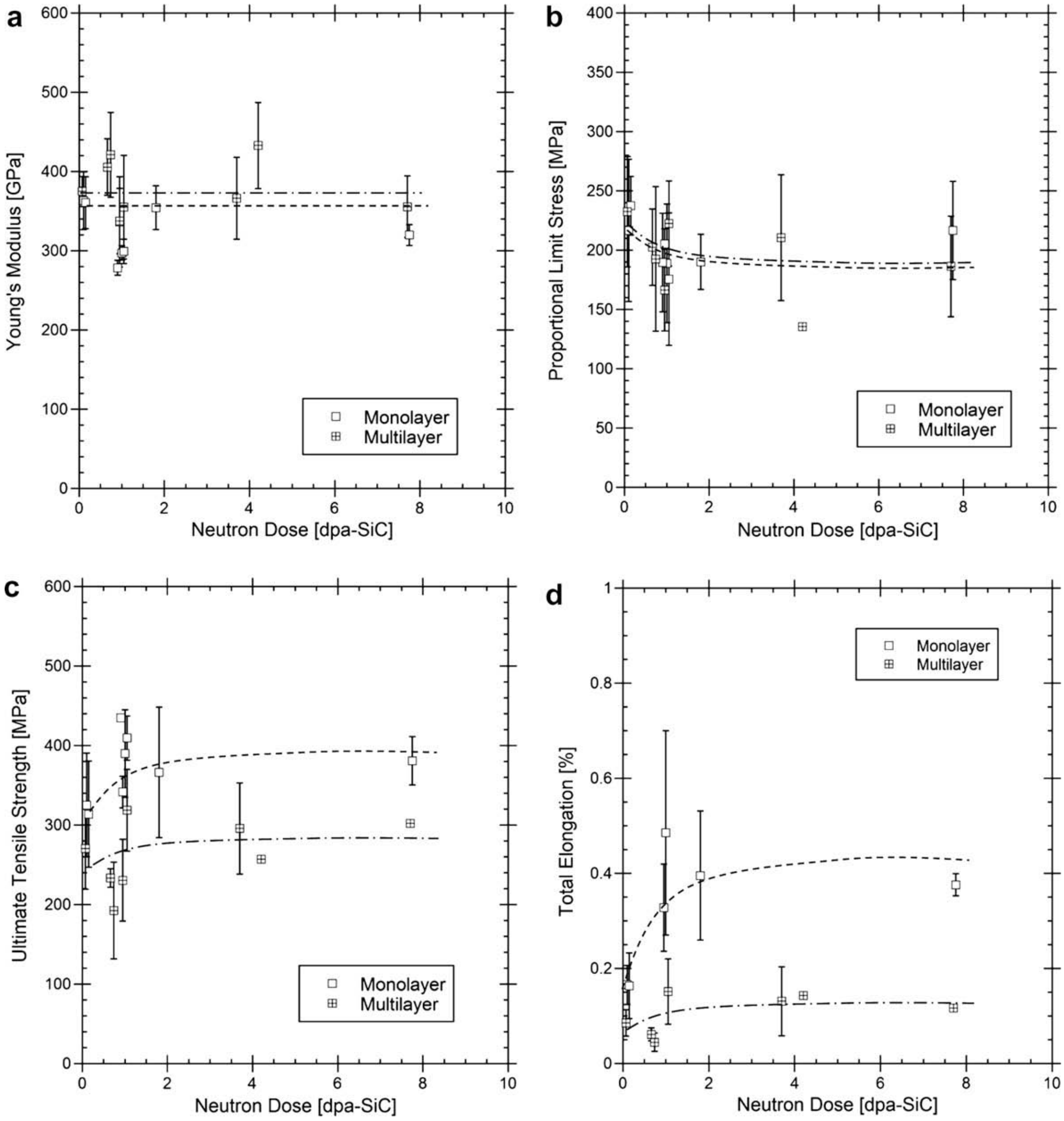

Fig. 4. Effects of neutron dose on (a) Young's modulus, (b) proportional limit stress, (c) ultimate tensile strength and (d) total elongation for unidirectional Hi-Nicalon™ Type-S/CVI-SiC composites with either a PyC monolayer or a PyC/SiC multilayer interphase.

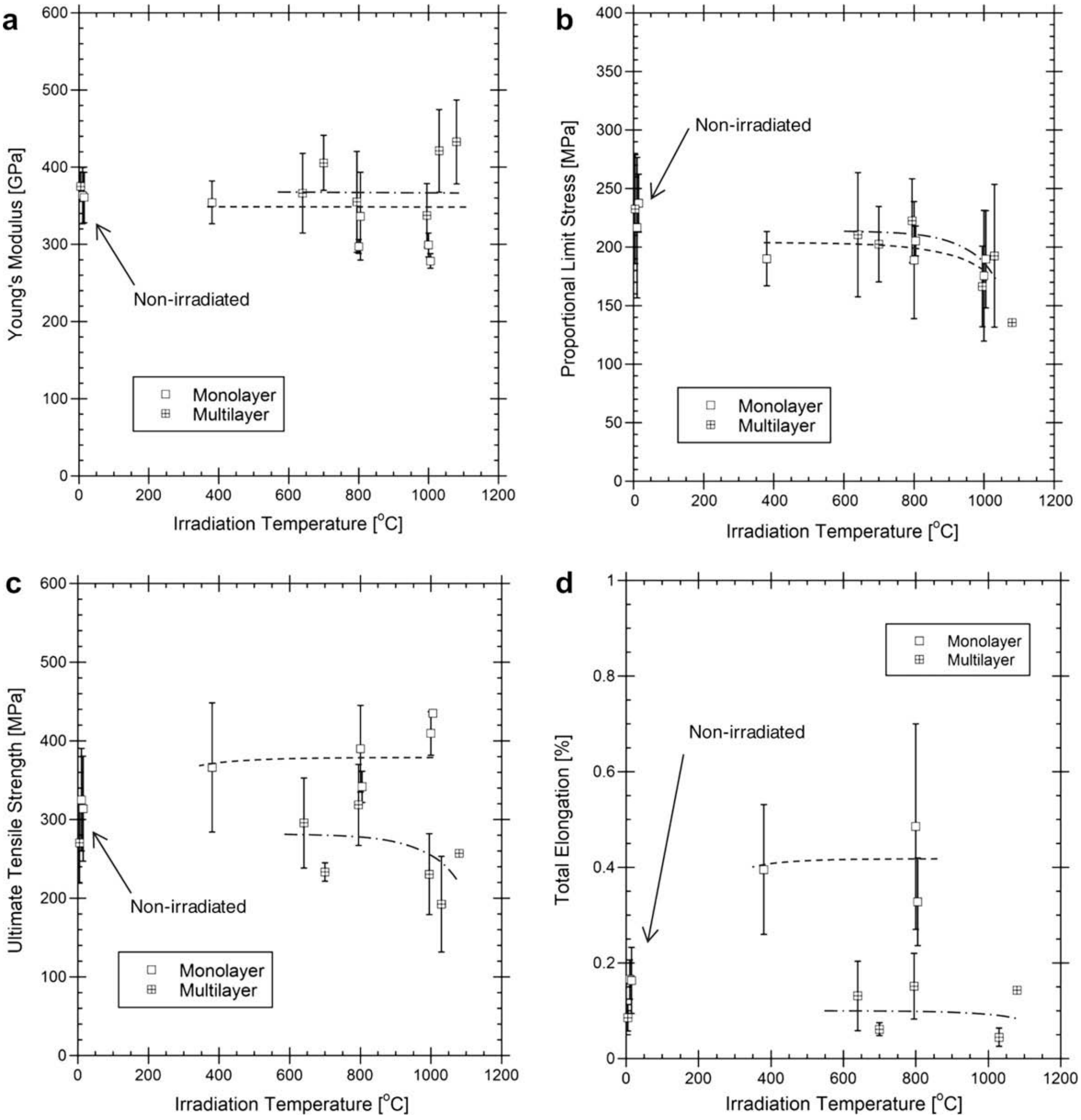

Fig. 5. Effects of irradiation temperature on (a) Young's modulus, (b) proportional limit stress, (c) ultimate tensile strength and (d) total elongation for unidirectional Hi-Nicalon™ Type-S/CVI-SiC composites with either a PyC monolayer or a PyC/SiC multilayer interphase. The data subsets of neutron dose range in 0.7–4.2 dpa were plotted.

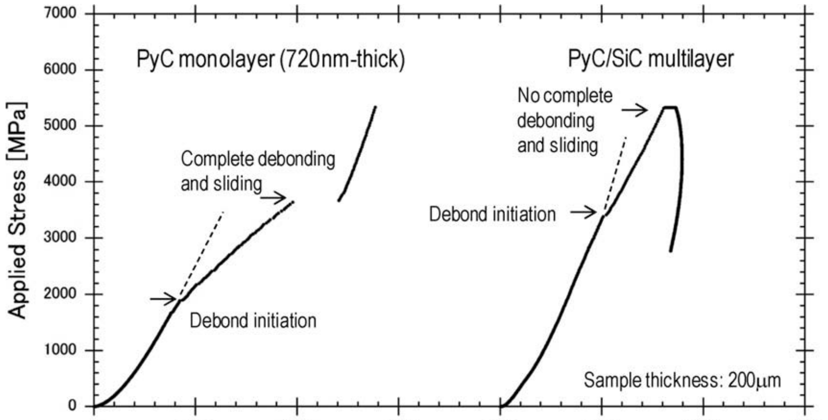

Fig. 6. Typical push-out fracture behaviors of Hi-Nicalon Type-S/CVI-SiC composites with either a PyC monolayer or a PyC/SiC multilayer interphase.

Table 4
Push-out test results for as-received and irradiated SiC/SiC composites.

Interphase	Irradiation condition	Sample thickness (μm)	Debond initiation stress (MPa)	Sliding stress (MPa)	# of valid tests
Monolayer	Non-irradiated (batch #1)	50	2871 (882)	2895 (892)	22
		100	2611 (1033)	3351 (1071)	33
		200	2875 (734)	–	18
	Non-irradiated (batch #2)	50	891 (423)	910 (440)	22
		100	1576 (619)	2071 (911)	31
		200	1870 (537)	4049 (917)	33
	0.8dpa 380 °C (HFIR-FUN)	53	1892 (642)	1965 (715)	23
		120	2458 (1168)	3362 (1415)	45
		153	3170 (886)	4238 (696)	24
		189	1940 (732)	2837 (1186)	13
		212	2645 (954)	4091 (891)	50
	1.8dpa 380 °C (HFIR-FUN)	58	863 (307)	1059 (398)	14
		87	1520 (265)	1646 (361)	30
		114	842 (400)	910 (457)	74
		145	1055 (245)	1155 (278)	22
	7.7 dpa 800 °C (HFIR-14J)	40	1186 (199)	1189 (198)	16
		80	1467 (311)	1712 (396)	23
		118	1680 (426)	2821 (823)	24
		210	1702 (284)	3544 (498)	10
Multilayer	Non-irradiated	30	3085 (835)	3085 (835)	5
		50	3554 (1090)	4205 (1107)	12
		100	3518 (680)	–	18
		200	3355 (830)	–	16
	0.7 dpa 740 °C (HFIR-NERI)	25	3006 (963)	–	49
		100	2974 (1027)	–	22
		137	3078 (1472)	–	26
		154	3323 (654)	–	22
	0.7 dpa 1030 °C (HFIR-NERI)	100	2198 (1119)	–	26
		150	3056 (773)	4985 (180)	25
		185	2155 (735)	–	25
	3.7 dpa 640 °C (HFIR-NERI)	40	2457 (982)	2870 (650)	17
		165	2836 (732)	–	24
		190	2619 (536)	–	24
	4.2 dpa 1080 °C (HFIR-NERI)	75	1789 (402)	2016 (62)	28
		150	2124 (692)	–	30
		210	2098 (375)	–	28
	7.7 dpa 800 °C (HFIR-14J)	60	2188 (399)	2223 (472)	21
		90	3040 (839)	–	18
		120	2550 (585)	–	33
		220	2982 (536)	–	22

Note: Numbers in parenthesis indicate one standard deviation.

Table 5
Interfacial shear properties of as-received and irradiated SiC/SiC composites.

Interphase	Irradiation campaign	Irradiation condition	Interfacial debond shear strength				Interfacial friction stress	
			High-density PyC case		Low-density PyC case		τ_s (MPa)	$\Delta\tau_s$ (%)
			τ_s (MPa)	$\Delta\tau_s$ (%)	τ_f (MPa)	$\Delta\tau_f$ (%)		
Monolayer	None (batch #1)	–	234 (45)	–	311 (47)	–	115 (21)	–
	None (batch #2)	–	125 (35)	–	172 (27)	–	61 (1)	–
	HFIR-FUN	0.8 dpa 380 °C	208 (36)	+16	267 (35)	+10	63 (8)	−28
	HFIR-FUN	1.8 dpa 380 °C	97 (14)	−46	165 (15)	−32	32 (8)	−64
	HFIR-14 J	7.7 dpa 800 °C	148 (15)	−18	185 (14)	−24	56 (6)	−36
Multilayer	None	–	338 (45)	–	424 (46)	–	267 (18)	–
	HFIR-NERI	0.7 dpa 740 °C	330 (51)	−2	402 (51)	−5	>210	<−21
	HFIR-NERI	0.7 dpa 1030 °C	240 (51)	−29	320 (50)	−25	100 (3)	−63
	HFIR-NERI	3.7 dpa 640 °C	279 (44)	−17	346 (43)	−18	215 (49)	−19
	HFIR-NERI	4.2 dpa 1080 °C	201 (28)	−41	270 (27)	−36	81 (2)	−70
	HFIR-14J	7.7 dpa 800 °C	277 (30)	−18	329 (29)	−22	111 (24)	−58

Note: Numbers in parenthesis indicate one standard deviation.

total thickness of the PyC layers was applied. As mentioned later, residual stresses at the interface for the multilayer composites are nearly compatible by taking the case of monolayer composites with a total thickness of multilayered PyC.

3. Results

3.1. Tensile properties

Fig. 3 shows typical stress–strain curves of non-irradiated and irradiated Hi-Nicalon™ Type-S/CVI-SiC composites with either a PyC monolayer or a PyC/SiC multilayer interphase and Table 3 lists reduced tensile properties. Data from an irradiation experiment in the Japan materials test reactor (JMTR, Oarai, Japan) for the identical materials are included [12]. Key common findings are summarized as follows: (1) very minor change in Young's modulus by irradiation, (2) enhanced quasi-ductility beyond the proportional limit, i.e., no embrittlement by irradiation, resulting in apparent increase of total elongation and (3) reduction of PLS. The tensile strength was nearly unchanged for monolayer composites at any irradiation temperatures. Similarly no significant decrease of UTS was observed for multilayer composites when $T_{\mathrm{irr}} < 1000$ °C, while minor reduction of UTS when $T_{\mathrm{irr}} > 1000$ °C was specified.

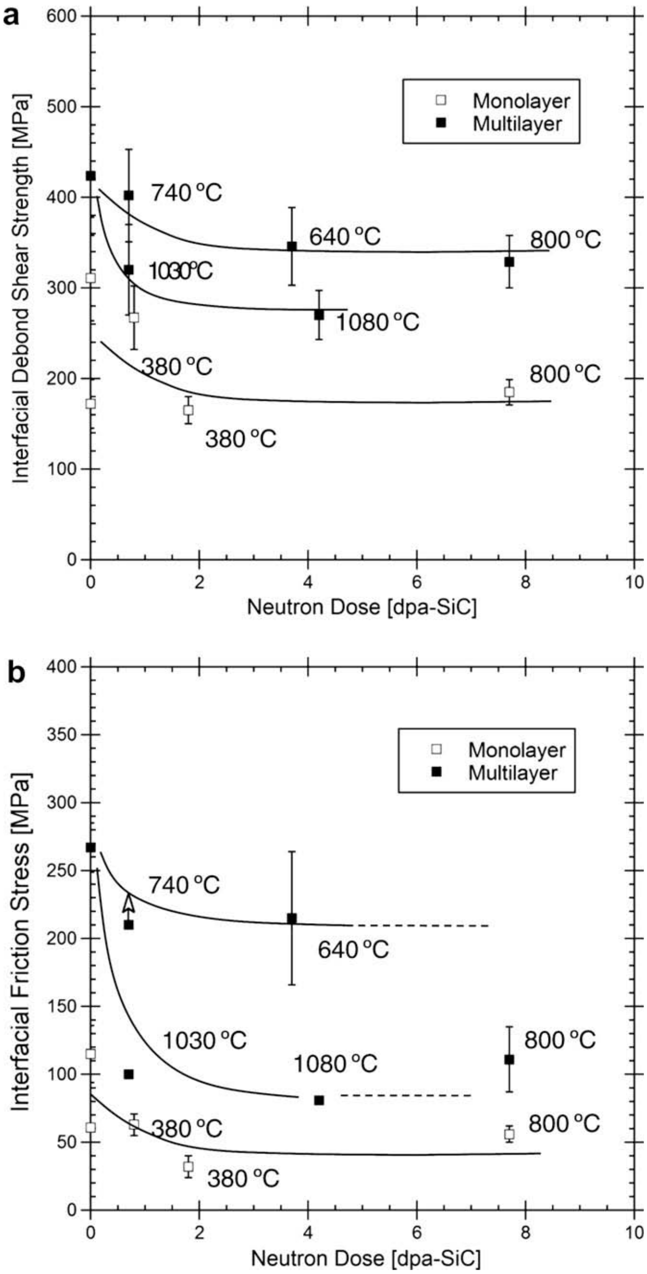

Fig. 7. Effects on neutron dose on (a) the interfacial debond shear strength and (b) the interfacial friction stress. Irradiation temperatures are noted in the figure. Irradiation-induced change of elastic properties of SiC and PyC was considered. No contribution from swelling was however considered. Glassy carbon was assumed.

Fig. 4 plots tensile data as a function of neutron dose. In the figure, error bars indicate ±1 standard deviation. The proportional limit tensile stress slightly decreases even at low neutron doses of ~0.7 dpa and approaches a constant (~200 MPa) with increasing neutron dose for both interphase types. Tensile strength and total elongation conversely tend to increase and approach a constant with increasing neutron dose. The increment of UTS for monolayer composites (~30%) was greater than that of multilayer composites (~20%). Similarly, the increment of total elongation for monolayer composites (~160%) was almost double of multilayer composites (~70%). Meanwhile, their Young's moduli seem nearly unchanged by irradiation. Large data scatter is due primarily to the variance of porosity and fiber volume fraction.

The data subsets in the fluence range of 0.7–4.2 dpa in Fig. 4 were extracted and separately plotted as a function of irradiation temperature (Fig. 5). In Fig. 5, Young's moduli for both interface structure types appeared unchanged by irradiation accounting for the wide data scatter (~30%). In contrast, the PLS slightly decreased after irradiation at all temperatures, however, the temperature-dependence seems very minor even at ~1000 °C. This is observed for both interphase types tested. Additionally, within the limited data set provided, it appears that a further decrease of the PLS has taken place when $T_{\mathrm{irr}} > 1000$ °C. Both UTS and total elongation were nearly unchanged by irradiation for multilayer composites when $T_{\mathrm{irr}} < 1000$ °C, while they significantly increased by irradiation for monolayer composites. When $T_{\mathrm{irr}} > 1000$ °C, a clear difference between the monolayer and multilayer composites was obtained: decreases of UTS for multilayer composites vs. no major deterioration for monolayer composites.

3.2. Interfacial shear properties

Fig. 6 shows comparison of typical load-displacement curves during fiber push-out process between monolayer and multilayer composites. As schematically shown in Fig. 2, the fiber push-out process generally has the following four stages: (1) elastic deformation with a tiny plastic deformation, (2) debond initiation at the interface from the loading surface, (3) progressive debond coupled with interfacial friction on the debonded fiber surface and (4) complete fiber debonding and sliding. When using a sharp indenter tip, the initial segment of the load-displacement curve becomes non-linear due to the plastic deformation below the indenter. Beyond debond initiation, the displacement rapidly increases and a load-displacement curve shows a secondary non-linear segment. In Fig. 6, a concave shape of the secondary non-linear segment for multilayer composites is due to the inherently high interfacial friction resulting from the rough surface of the fiber. The limited load capacity of the test system does not allow the complete debonding and sliding of the composites with exceptionally high debond initiation stress. More than 80% of measurements of $\sigma_{\max}$ for multilayer composites were invalid when specimen thickness was >100 μm. The slightly convex shape observed for monolayer composites is due to the comparably low friction stress. A plateau beyond complete debonding, i.e., sliding of the pushed-out fiber, was observed for the case of thick PyC monolayer composites. The further load increment after complete sliding indicates a physical contact of the indenter sides with the SiC matrix when using a conic indenter.

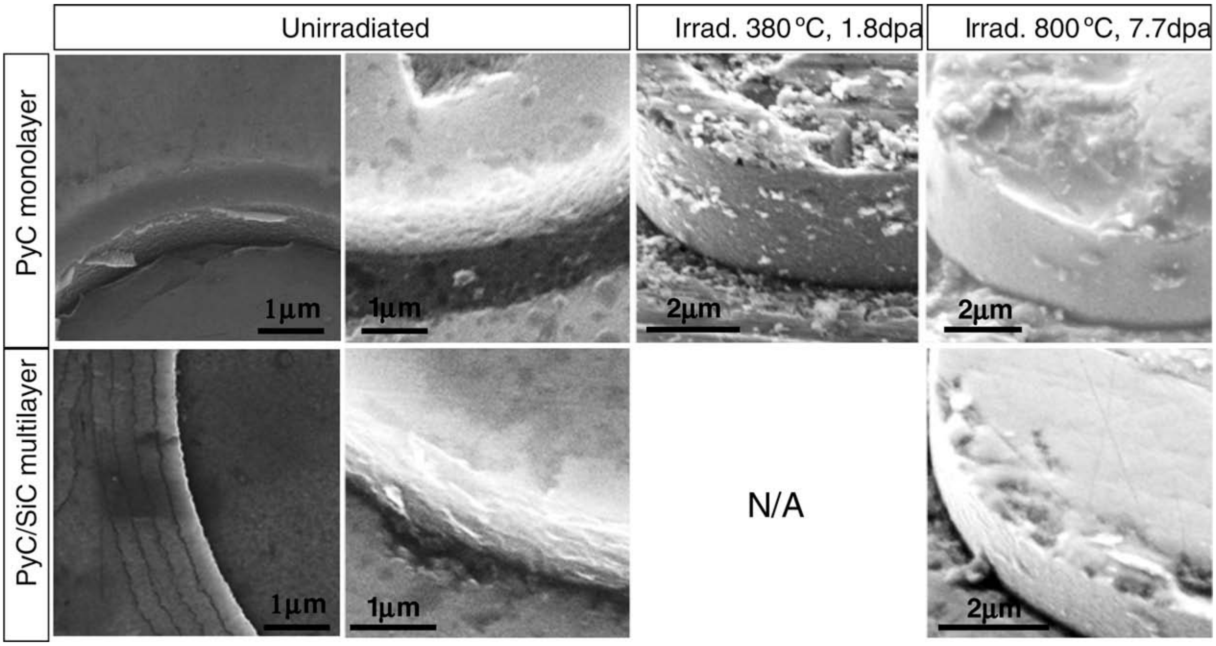

Fig. 8. Typical micrographs of pushed-out fiber surfaces under various irradiation conditions.

The least-square fits by Eqs. (1) and (4) can provide an interfacial debond shear strength (τ_s) and an interfacial friction stress (τ_f), respectively, from the experimental push-out data in Table 4. Table 5 lists τ_s and τ_f of monolayer and multilayer composites and Fig. 7 plots interfacial shear property data as a function of neutron dose (for the low-density PyC case). Note that the preliminary analysis in this study disregarded the contribution from swelling because the actual swelling in composite forms depend significantly on irradiation assisted stress relaxation; The importance of irradiation creep was pointed out by the bend stress relaxation test by Katoh et al. [43]. The anisotropic swelling of SiC under stress has also been reported [44]. Considering precisely the effect of irradiation-induced dimensional change with combined effects of dynamic irradiation effects is presently very difficult due to many uncertain factors and scarcity of data. Meanwhile, simple estimation by applying a minimum value of σ_{max} gives a lower limit ($\tau_f > 210$ MPa) as plotted in the figure with an arrow in Fig. 7, although the interfacial friction following irradiation at 740 °C up to 0.7 dpa could not be quantified due to the load limitation of the test system.

From Fig. 7, it is apparent that shear properties at the F/M interface depend on neutron dose. They apparently changed after irradiation, however, the dose dependence is not so significant when $T_{irr} = \sim 1080$ °C. Both τ_s and τ_f decrease by irradiation in low dose region and remain nearly unchanged with further increasing neutron dose regardless of the interface structure types, e.g. monolayer or multilayer. Of particular emphasis is that both τ_s and τ_f for multilayer composites were most affected when $T_{irr} = \sim 1080$ °C. However, it is worth noting that the interfacial shear properties for irradiated multilayer composites are still above average for monolayer composites. Even if the interfacial shear stresses decrease by irradiation, the high shear strength is still sufficient for the load-sharing at the F/M interface. Presently, no irradiation data is available for monolayer composites when $T_{irr} > 1000$ °C and therefore it should be noted that it is unclear whether this is specific to the multilayer interface case. Another uncertainty to be pointed out is a reduction of interfacial friction by irradiation at 800 °C up to 7.7 dpa for multilayer composites.

Fig. 8 exhibits typical micrographs of pushed-out fiber surfaces of as-received and neutron-irradiated materials. Importantly the primary crack occurred in the inner most PyC layer adjacent the fiber for both cases. For monolayer composites, there was no significant change in cracking path by neutron irradiation. The pushed-out fiber surfaces were smooth regardless of the irradiation, indicating crack propagation along the fiber surface. In contrast, the rough fiber surface for the as-received multilayer composites implies crack propagation within PyC interphase adjacent the fiber. The changing crack path: the crack path 'within' interphase before irradiation vs. the crack path 'along' the fiber/carbon interface after irradiation (7.7 dpa at 800 °C) was identified.

4. Discussion

4.1. Clamping stresses at the fiber/matrix interface

Interfacial shear properties are significantly dependent on residual compressive (clamping) stresses induced at the F/M interface. These clamping stresses are generally induced by the thermal expansion mismatch among the fiber, F/M interphase and matrix, and by roughness of the fiber surface [20]. Additionally, the secondary stresses induced by swelling and stress relaxation by irradiation creep may impose added complexity under neutron irradiation. For advanced SiC/SiC composites, the fiber and matrix are highly-crystalline SiC and it has been believed that their irradiation effects are essentially similar. However, recent study identified some differences in defect accumulation between fibers and purer SiC matrix, implying potential difference in swelling [41], which probably gives a residual stress at the F/M interface by irradiation. In spite of the presence of CTE mismatch between the SiC fiber and matrix, dose-dependent dimensional change of PyC would inevitably impose substantial stresses at the F/M interface [26]. In short, the radiation-induced stresses would undoubtedly influence the results and ultimately need to be considered.

A clamping stress working at the F/M interface can be qualitatively predicted under the simple assumption by adopting the four-phase (fiber core/PyC interphase/SiC matrix/composites) cylinder model [45–47]. This model discusses (1) anisotropy of the constituents, (2) the effect of interlayer thickness, (3) contributions from the thermal expansion mismatch and (4) irradiation effects. Of many models, the analytical method proposed by Oel [47] is adopted due to the perceived applicability to the multilayered interphase structure. In the following analysis, isotropic swelling of SiC and PyC was assumed. As aforementioned, quantification of the contribution of irradiation creep is very complicated for several reasons, therefore this study did not take this into account for simplicity.

Fig. 9 shows comparison of calculated thermal residual stresses in the radial and axial directions for monolayer and multilayer composites with respect to the radial distance from the fiber center. By taking data listed in Table 2, a residual tensile stress is induced in the radial direction. In the axial direction, a residual tensile stress is in the fiber, while a residual compression stress is in the matrix. However, because the manufacturer-claimed thermal expansion coefficients of Hi-Nicalon™ Type-S and PyC in Table 2 are uncertain, the effect of variation of CTEs of the fiber, F/M interphase and matrix on clamping stresses was first examined. Fig. 10 shows typical analytical results of residual radial stresses with respect to PyC interlayer thickness. It is apparent that the residual stress at the interface depends significantly on PyC interlayer thickness. The differential thermal expansion between the fiber and the matrix determines the direction of the stress at the F/M interface, i.e., residual compression when $\alpha_f < \alpha_m$ or tension when $\alpha_f > \alpha_m$. In contrast, the magnitude of the CTE of PyC imposes stress deviation with increasing PyC interlayer thickness. For instance, with a higher CTE of carbon assumed, e.g., high-density PyC, a residual stress becomes much more tensile and vice versa. Considering the hysteresis analysis [48] for stress–strain curves of non-irradiated composites in Fig. 3, the thermal residual stress in the radial direction becomes zero or slightly tensile for advanced SiC/SiC composites. It is therefore suggested that the CTE of Hi-Nicalon™ Type-S should be very close to or slightly higher than that of CVD-SiC. From these facts, a negative contribution to clamping at the interface is therefore anticipated. In contrast, the huge contribution to the interfacial shear strength during the fiber pull-out stage was generally induced by the improved surface roughness of the advanced SiC fiber. The fiber roughness influences the radial stress for debonded interface in a simple assumption [20]. Fig. 11 shows an example of analytical results of residual radial stresses by assuming a fiber surface roughness of $10 \sim 20$ nm. From Fig. 11, the rougher fiber surface can theoretically induce more compressive (clamping) stress. Specifically, a radial compressive stress increases for thinner PyC interlayer thickness.

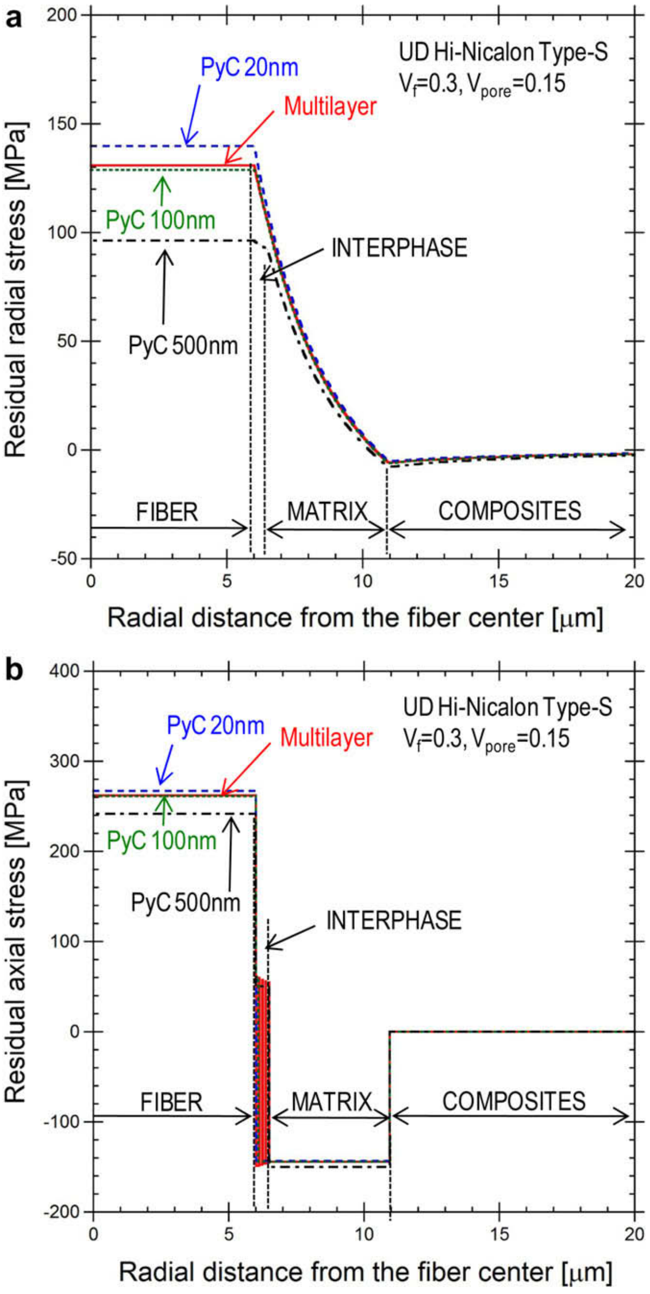

Fig. 9. Calculated thermally induced residual stresses: (a) radial stresses and (b) axial stresses.

In Fig. 9, another remark to be addressed is that the stress state in the multilayer composites is nearly identical to that of monolayer composites with a PyC interlayer thickness of the total PyC sub-layers of the multilayer. From this fact, the approximation incorporating the total PyC thickness will be fairly reasonable for the analysis of thermal residual stress in multilayer composites. In contrast, there is no doubt that the innermost PyC layer (adjacent the fiber) is important in an interface design to control crack propagation behavior because of the fact that a critical crack propagates along the fiber surface. From Fig. 8, the primary crack propagates along the surface of the first PyC layer. For the analysis of multilayer composites, it should therefore be reasonable to adopt the first PyC interlayer thickness and the total PyC interlayer thickness for a crack propagation analysis and a residual stress analysis, respectively.

Under neutron irradiation, residual stresses can be further induced by differential swelling among the fiber, F/M interphase and matrix. Fig. 12 shows an example of the analysis of irradiation-induced residual radial and axial stresses at the F/M interface. In Fig. 12, the input data of the swelling and Young's moduli for irradiated SiC and high-density PyC were taken from the estimates by empirical equations as listed in Table 2. This analysis assumes no change of CTE by irradiation. No contribution from irradiation creep was also considered for simplicity. Preliminary analysis in Fig. 12 suggests that neutron irradiation enhances more tensile residual stress at the F/M interface in the radial (clamping) direction. It should be also noted that (1) the radiation-induced residual stresses for thick PyC monolayer composites are potentially larger than that of thin-layered multilayer composites and (2) no significant influence of irradiation temperature would be analytically anticipated. The tensile hysteresis curves for irradiated composites in Fig. 3 may support these phenomena. From Fig. 12, it is obvious that there exists a stress peak around a few dpa corresponded with 'turn-around' of the swelling behavior of PyC. This result is quite similar to the trend suggested from the preliminary evaluation by Henager et al. [49]. Presently no analysis can be done for the low-density PyC case because of limited data availability. Nevertheless, considering many similarities with high-density PyC, it is likely that the radiation-enhanced densification of the low-density

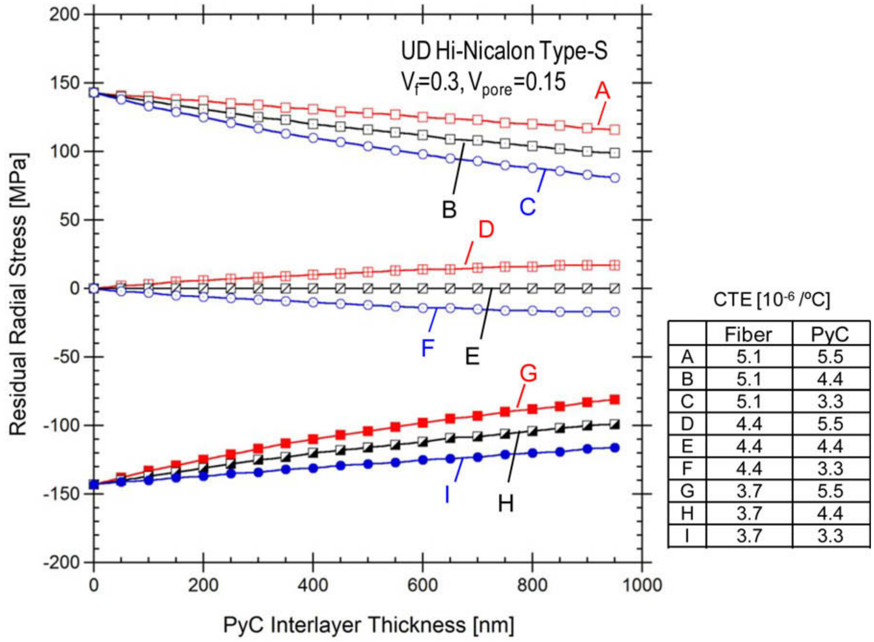

	Fiber	PyC
A	5.1	5.5
B	5.1	4.4
C	5.1	3.3
D	4.4	5.5
E	4.4	4.4
F	4.4	3.3
G	3.7	5.5
H	3.7	4.4
I	3.7	3.3

Fig. 10. Effect of the fiber surface roughness on residual radial stress at the F/M interface. In calculation, the fixed CTEs were applied: 4.4 × 10^{-6}/°C for the matrix and 5.1 × 10^{-6}/°C for the fiber.

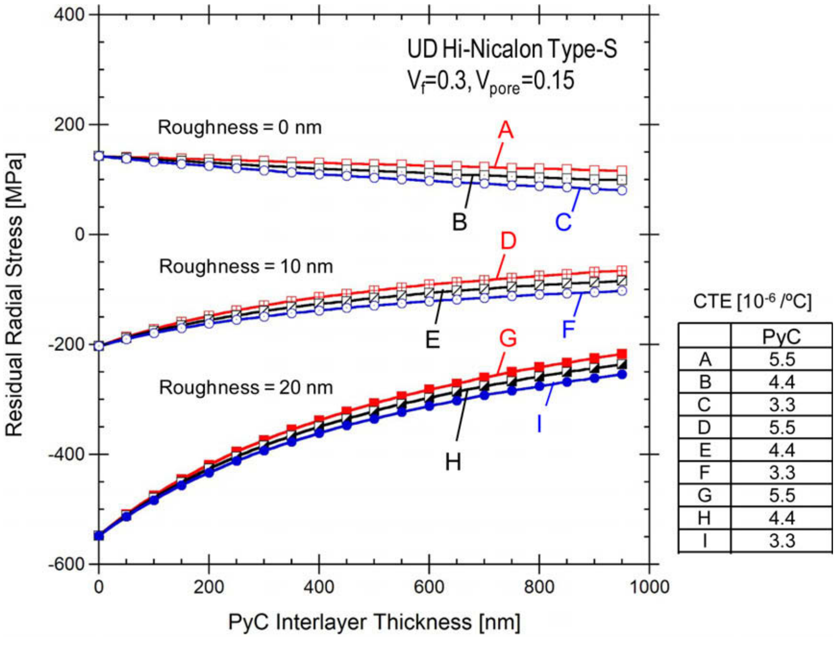

	PyC
A	5.5
B	4.4
C	3.3
D	5.5
E	4.4
F	3.3
G	5.5
H	4.4
I	3.3

Fig. 11. Thermal residual stresses at the F/M interface vs. PyC interlayer thickness with varied CTEs of the fiber and interphase. In calculation, the CTE of 4.4 × 10^{-6}/°C was fixed for the matrix.

PyC induces residual tensile stresses at the interface. From the limited swelling data in [35], no clear turn-around would, however, be anticipated. In contrast, the axial stresses in the fiber and matrix become much more tensile and compressive by neutron irradiation, respectively. Specifically, the axial stress in the matrix analytically saturates with increasing neutron dose (Fig. 12).

4.2. Effect of neutron irradiation on interfacial shear properties

In preliminary work by the authors [13], the effect of swelling on the F/M interfacial strength was disregarded because it has been believed that the condition under which irradiation-induced swelling would not become a critical concern. However, this may not be an appropriate assumption, especially in the low neutron dose range, in which swelling-induced stress would become analytically significant (Fig. 12). However, there might not be a critical concern considering stress relaxation by irradiation creep. For the evaluation on the interfacial shear properties, this residual stress issue, therefore, needs to be clarified first of all. Though the importance of irradiation-induced stresses is recognized, their contribution cannot be quantified completely at this moment since understanding of the swelling behavior and irradiation creep is insufficient.

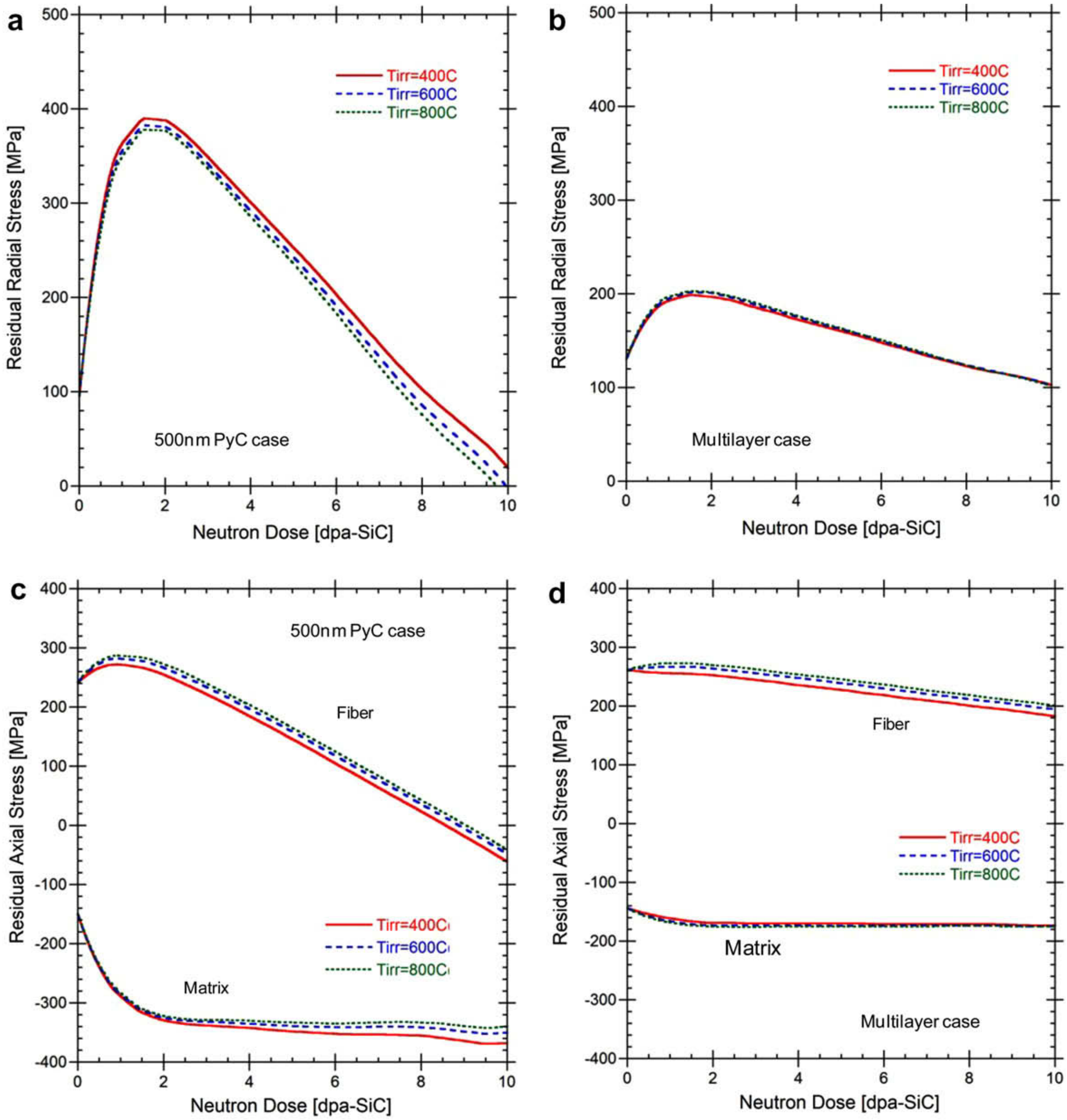

Fig. 12. Calculated irradiation-induced stresses: (a) radial stress for monolayer, (b) radial stress for multilayer, (c) axial stress for monolayer and (d) axial stress for multilayer composites. In calculation, radiation-induced changes in swelling and Young's moduli of the fiber, matrix and interphase were empirically considered. The effect of irradiation creep was ignored for simplicity. The fiber volume fraction and porosity are 30% and 15%, respectively.

The interfacial shear strength data preliminarily defined in this study therefore indicates a probable maximum shear strength at the F/M interface of irradiated SiC/SiC composites. Because of the existence of potential irradiation-induced radial tensile stresses at the F/M interface, the interfacial shear properties may decrease. However, considering stress relaxation by irradiation creep, such degradation would be smaller than expected. An important conclusion obtained under this assumption is that the interfacial shear strength undoubtedly decreases by neutron irradiation. Of particular emphasis is that, regardless of the interface type, e.g., monolayer or multilayer, the effect of neutron irradiation on interfacial shear properties appears to be very similar when $T_{irr} < 1000$ °C. Interfacial shear properties decrease first at lower neutron doses and eventually approach a constant. Importantly, it can be interpreted as irradiation-induced change of the interfacial shear strength dependent on irradiation-induced dimensional change of carbon interphase. When $T_{irr} > 1000$ °C, further deterioration of interfacial shear properties would be anticipated.

The only anomaly data to be pointed out is degradation of the interfacial friction at 800 °C up to 7.7 dpa for multilayer composites. Under this irradiation condition, no serious irradiation-induced stress at the F/M interface is expected (Fig. 12). Alternatively, the great portion of the clamping stresses is attributed to the friction from the rough surface at the sliding plane. As aforementioned, the microstructure of PyC near the fiber is more graphitic rather than turbostratic isotropic carbon [38], possibly giving a relatively weak shear spot around graphitic PyC. Indeed, a micrograph identified that a primary crack propagated near the fiber/interphase interface even for very thick PyC interphase composites (Fig. 8). For thin-layered multilayer composites, a primary crack should propagate with a connection of two weak interfaces: the fiber/PyC and PyC/1st SiC matrix interfaces. This would be supported by the fact that flake-like PyC debris has been observed in a tensile fractured surface of the multilayer composites (Fig. 13). Such crack propagation produces a rough crack plane, giving a strong friction at the debonded interface. It is generally reported

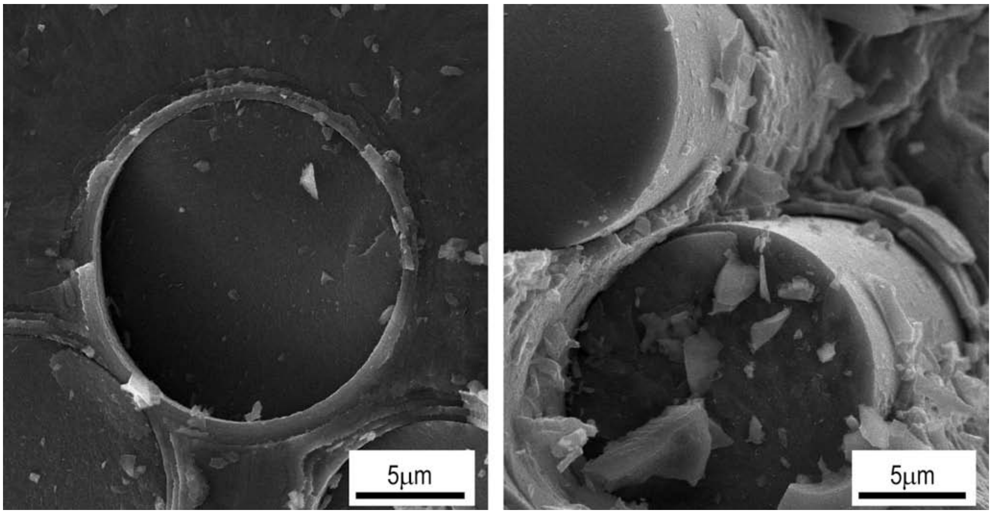

Fig. 13. Typical tensile fracture surfaces of multilayer interphase composites.

that interfacial shear properties are significantly improved when applying advanced SiC fibers with rough surface [50] or modified SiC fibers with surface treatment [51]. From Fig. 8, it is no doubt that the frictional stress of multilayer composites at 800 °C up to 7.7 dpa decreased remarkably due to the fact that the crack path changed from the rough surface within PyC to the smooth fiber surface. However, this data point is quite questionable because there is no reasonable answer whether it is actually a phenomenon induced by neutron irradiation by considering scarcity of data and by simply extrapolating the data trend. Also, no clear mechanism has yet been proven. It is necessary to clarify the detailed crack propagation behavior to conclude it.

Another important point of discussion is the observed deterioration of interfacial shear properties by high-temperature neutron irradiation. From Fig. 12, no significant difference of irradiation-induced residual stresses was generally expected with the change of irradiation temperatures. However, in Fig. 7, it is apparent that irradiation-induced deterioration of interfacial shear stresses enhanced at >1000 °C. According to the finding by Kondo et al. [52], this temperature (~1050 °C) agrees well with the temperature at which irradiation-induced voids can be detected, however, it is proven that the void contribution to swelling is negligibly small under this condition. Accordingly, no deterioration of pure SiC was identified [4]. In contrast, there is a report that the strength of bare Hi-Nicalon™ Type-S fiber itself deteriorates by irradiation near 1000 °C due probably to the presence of uncertain impurities identified by mass analysis [41]. However, there is also evidence that the fiber strength was retained during irradiation in composite samples [41]. The fiber deterioration by irradiation would therefore be unlikely. Alternatively, irradiation creep, which has recently been seen for SiC [43], may influence the irradiation behavior of SiC/SiC composites. Relaxation of residual stresses by irradiation creep would be greater in case of lower temperature irradiation. Otherwise, deterioration of the PyC interphase itself at higher temperature irradiation is possible but there is no evidence for this at present.

4.3. Effect of interfacial shear properties on tensile properties

The composites' overall performance relies on the F/M interfacial properties, as well as fiber strength itself. In particular for unidirectional composites, the proportional limit stress can be described as a function of the fiber volume fraction, an interfacial debond energy, a matrix fracture energy, and a misfit stress for the bonded F/M interface case [53]. The matrix fracture energy is unaffected or slightly increased by irradiation [4,54], resulting in minor contribution for the PLS decrease. In contrast, the interfacial debond energy, closely related to the interfacial debond shear strength, varies by irradiation and this would therefore be a possible contributor. Recent updates in Tables 3 and 5 provide a qualitatively good correlation among the interfacial debond shear strength and the PLS. Additionally, the reportedly higher CTE of Hi-Nicalon™ Type-S as compared to CVD-SiC may cause an intrinsic thermally-induced residual stress, providing a misfit stress at the interface (Fig. 9). A thermally-induced compressive axial stress in the matrix theoretically increases PLS. Under this condition, irradiation creep should eliminate this stress to compensate it. Thus, irradiation creep may decrease PLS, ignoring the differential axial swelling. This is qualitatively in good agreement with the results. Potentially, the irradiation-induced residual stress (Fig. 12) might increase the PLS. This is, however, quite opposite from the actual trend. Stress relaxation by irradiation creep may also affect the results even in this case. The PLS also depends on Young's moduli of the fiber, matrix, and composites. The change of Young's moduli of SiC by irradiation is, however, statistically very small at high-temperatures ~1000 °C [4] and this effect would be negligible.

The effect of neutron irradiation on interfacial shear properties was also discussed from the tensile unloading–reloading hysteresis loop analysis for the same-grade composites [55]. In that study, enlarged hysteresis loop width first implied a probable decrease of interfacial friction by irradiation. However, considering the fact that push-out tests in this study show no significant deterioration of interfacial friction up to 7.7 dpa at 800 °C for monolayer composites [13], it was concluded that this mechanism is insufficient to explain the phenomenon completely. Alternatively, it is believed that the hysteresis loop widening is due primarily to the difference in matrix crack density. The higher matrix crack density for irradiated samples gives the wide hysteresis loop. The matrix crack density increases with decreasing interfacial debond shear strength. For multilayer composites, because sufficient hysteresis information could not be provided due to the extremely low strain after matrix cracking, much discussion could not be done based on that.

It is well known that a weak interface leads to lower composite strengths since some fibers are never loaded to their full capacity and that some fibers fail prior to achieving full fracture strength if their interface is too strong. The fracture strength is, therefore, dependent on the interfacial shear stresses as well as the fiber strength. This is reasonable based on the analytical result by Curtin

[56]. The fracture strength of composites can be determined by the Weibull characteristic strength, which depends on both fiber strength and interfacial friction stress, the Weibull modulus, and volume fraction of the fibers. It is reported that the Weibull modulus slightly decreases by irradiation [10,41], however this would not have a large impact on the results (<5% decrease change due to irradiation). The increment of the post-irradiation strength of the composites for $T_{\mathrm{irr}} < 1000$ °C is contrarily attributed to the modification of the fiber strength by irradiation [10]. This is supported by the known presence of irradiation-assisted toughening of SiC [4,54]. In these reports, the potential surface modification, relaxation of the machining-induced local stress, modifications of elastic properties and fracture energy by irradiation was believed to explain the improved fracture toughness, giving a positive contribution to the composite strength. Another report did not show any degradation of strength for 2D SiC/SiC composites at ~1100 °C [41]. In conclusion, the primary contributor for the deterioration of the composite strength by high-temperature neutron irradiation ($T_{\mathrm{irr}} > 1000$ °C) is moderate degradation of the interfacial friction stress.

5. Conclusions

The performance of composites depends on the F/M interphase. This study aims to investigate the effect of neutron irradiation on interfacial shear properties of unidirectional Hi-Nicalon™ Type-S/CVI-SiC composites with either a PyC monolayer or a PyC/SiC multilayer interphase. For that purpose, tensile and single fiber push-out test techniques were applied. Key findings are summarized as follows:

1. For the neutron fluence and irradiation temperature range studied, the interphase degradation, which is measurable but not so dramatic, did not compromise the overall mechanical performance of the composites. The interphase was still capable of carrying out its dual roles of toughening and load transfer.
2. Multilayer composites exhibit comparably higher interfacial shear stresses than monolayer composites even after neutron irradiation due to the thin innermost PyC layer. Even though there is a difference in magnitude of the strength between monolayer and multilayer composites, both an interfacial debond shear strength and an interfacial friction stress decrease by neutron irradiation dependent on the neutron fluence. Such irradiation-induced decrease of interfacial shear properties is due primarily to the irradiation behavior of the interphase material, i.e., PyC.
3. Dependence of irradiation temperature seems very minor at <1000 °C for both interphase types. Considerable reduction of interfacial shear stresses was contrarily identified for multilayer composites by high-temperatures neutron irradiation ($T_{\mathrm{irr}} > 1000$ °C). However, it cannot be concluded whether this deterioration is specific to the multilayer composites or not. Due to the scarcity of data, deterioration of interfacial shear stresses at high-temperatures for monolayer composites is uncertain.
4. The proportional limit tensile stress is closely linked to the radiation-induced change of the interfacial shear stresses, while the tensile strength of the composites for the conditions studied was nearly unaffected by neutron irradiation.

Acknowledgements

The authors would like to thank Dr R.J. Shinavski for fabricating materials, and Dr J.T. Busby, Ms A.M. Williams and Ms P.S. Tedder for post-irradiation experiments. The special thanks are extended to Dr T.S. Byun for reviewing the manuscript. Additionally, the authors would like acknowledge the use of the High Flux Isotope Reactor user facility. This research was sponsored by the Office of Fusion Energy Sciences, US Department of Energy under contract DE-AC05-00OR22725 with UT-Battelle, LLC and by the US Department of Energy Office of Nuclear Energy, Science and Technology, a Nuclear Energy Research Initiative (NERI) Project, under Contract NEAF355 (AF3510) with Oak Ridge National Laboratory (operated by UT-Battelle, LLC). This study was also a part of 'JUPITER-II' US-Department of Energy/Japanese Ministry of Education, Culture, Sports, Science and Technology (MEXT) collaboration for fusion material system research.

Appendix A

To determine the interfacial debond shear strength (τ_s) from the experimentally determined interfacial debond initiation stress (σ_d), a non-linear double shear-lag model for the transversely isotropic coordination was proposed. The double shear-lag model assumes three phases, i.e., a fiber, an interphase, and a composite (Fig. A1). In the model, radii of the fiber, interphase and composites are denoted as r_f, r_i, and r_c, respectively. The important update from the published models is that the modified model can consider anisotropy of each constituent. Elastic moduli in the axial and radial directions are E_z and E_r, respectively. Similarly Poisson's ratios of ν_z and ν_r, thermal expansion coefficients of α_z and α_r, irradiation-induced strains of ε_z and ε_r are defined. The axial shear modulus is also defined as G_{44}. In the following discussion, superscripts of f, i, and c indicate the fiber, interphase and composites, respectively. The temperature difference from the fabrication temperature is denoted as ΔT.

On the basis of previous works [22,25], the coefficients in Eq. (1) are determined as follows:

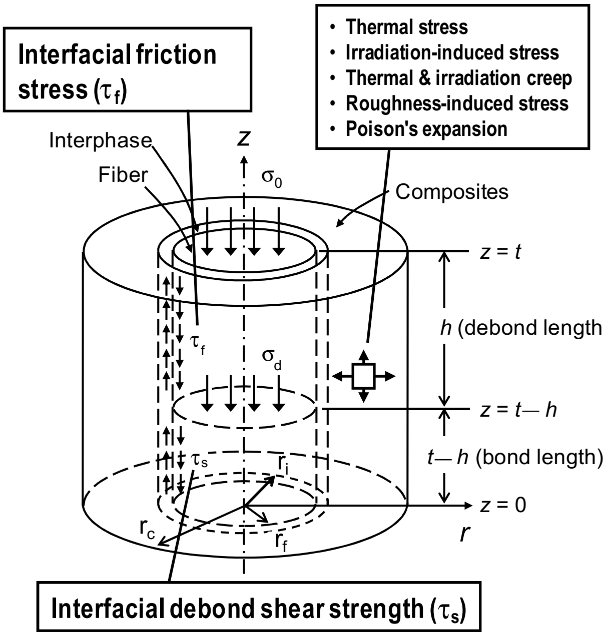

Fig. A1. Schematic illustration of transversely isotropic composites system for determination of the interfacial debond shear strength (τ_s) and the interfacial friction stress (τ_f).

$$\lambda=\frac{1}{r_{\mathrm{f}}}\left[\frac{-X_2+\left(X_2^2-4X_1X_3\right)^{1/2}}{2X_1}\right]^{1/2} \tag{A1}$$

$$Z=\frac{E_z^{\mathrm{f}}(S_{21}-S_{11})}{(A_5+A_6)\left[\nu_z^{\mathrm{f}}(S_{23}-S_{13})-(S_{24}-S_{14})\right]-E_z^{\mathrm{f}}(S_{21}-S_{11})} \tag{A2}$$

$$\begin{aligned}\sigma_{\mathrm{th}}={}&\frac{A_2(A_5+A_6)}{A_1}\left[\frac{\nu_z^{\mathrm{f}}(S_{23}-S_{13})-(S_{24}-S_{14})}{E_z^{\mathrm{f}}(S_{21}-S_{11})}-\frac{1}{A_5+A_6}\right]\\&\times\left[(S_{23}-S_{13})\left(\alpha_r^{\mathrm{i}}-\alpha_r^{\mathrm{f}}\right)+(S_{24}-S_{14})\left(\alpha_z^{\mathrm{i}}-\alpha_z^{\mathrm{f}}\right)+(S_{25}-S_{15})\left(\alpha_r^{\mathrm{c}}-\alpha_r^{\mathrm{i}}\right)\right.\\&\left.+(S_{26}-S_{16})\left(\alpha_z^{\mathrm{c}}-\alpha_z^{\mathrm{i}}\right)\right]\Delta T\end{aligned} \tag{A3}$$

$$\begin{aligned}\sigma_{\mathrm{irr}}={}&\frac{A_2(A_5+A_6)}{A_1}\left[\frac{\nu_z^{\mathrm{f}}(S_{23}-S_{13})-(S_{24}-S_{14})}{E_z^{\mathrm{f}}(S_{21}-S_{11})}-\frac{1}{A_5+A_6}\right]\\&\times\left[(S_{23}-S_{13})\left(\varepsilon_r^{\mathrm{i}}-\varepsilon_r^{\mathrm{f}}\right)+(S_{24}-S_{14})\left(\varepsilon_z^{\mathrm{i}}-\varepsilon_z^{\mathrm{f}}\right)+(S_{25}-S_{15})\left(\varepsilon_r^{\mathrm{c}}-\varepsilon_r^{\mathrm{i}}\right)\right.\\&\left.+(S_{26}-S_{16})\left(\varepsilon_z^{\mathrm{c}}-\varepsilon_z^{\mathrm{i}}\right)\right]\end{aligned} \tag{A4}$$

where

$$A_1=\frac{\frac{2r_{\mathrm{f}}^2}{r_{\mathrm{i}}^2-r_{\mathrm{f}}^2}\ln\left(\frac{r_{\mathrm{i}}}{r_{\mathrm{f}}}\right)-1}{\frac{2r_{\mathrm{i}}^2}{r_{\mathrm{i}}^2-r_{\mathrm{f}}^2}\ln\left(\frac{r_{\mathrm{i}}}{r_{\mathrm{f}}}\right)-1} \tag{A5}$$

$$A_2=\frac{2G_{44}^{\mathrm{i}}}{E_z^{\mathrm{i}}\left[\frac{2r_{\mathrm{i}}^2}{r_{\mathrm{i}}^2-r_{\mathrm{f}}^2}\ln\left(\frac{r_{\mathrm{i}}}{r_{\mathrm{f}}}\right)-1\right]} \tag{A6}$$

$$A_3=\frac{2G_{44}^{\mathrm{c}}}{E_z^{\mathrm{c}}\left[\frac{2r_{\mathrm{c}}^2}{r_{\mathrm{c}}^2-r_{\mathrm{i}}^2}\ln\left(\frac{r_{\mathrm{c}}}{r_{\mathrm{i}}}\right)-1\right]} \tag{A7}$$

$$A_4=\frac{\frac{2r_{\mathrm{i}}^4}{r_{\mathrm{f}}^2\left(r_{\mathrm{i}}^2-r_{\mathrm{f}}^2\right)}\ln\left(\frac{r_{\mathrm{i}}}{r_{\mathrm{f}}}\right)-\frac{3r_{\mathrm{i}}^2-r_{\mathrm{f}}^2}{2r_{\mathrm{f}}^2}}{\frac{2r_{\mathrm{i}}^2}{r_{\mathrm{i}}^2-r_{\mathrm{f}}^2}\ln\left(\frac{r_{\mathrm{i}}}{r_{\mathrm{f}}}\right)-1} \tag{A8}$$

$$A_5=\frac{G_{44}^{\mathrm{c}}E_z^{\mathrm{i}}\left[\frac{r_{\mathrm{i}}^2-r_{\mathrm{f}}^2}{r_{\mathrm{f}}^2}-\frac{r_{\mathrm{i}}^2+r_{\mathrm{f}}^2}{r_{\mathrm{f}}^2}\ln\left(\frac{r_{\mathrm{i}}}{r_{\mathrm{f}}}\right)\right]}{G_{44}^{\mathrm{i}}E_z^{\mathrm{c}}\left[\frac{2r_{\mathrm{i}}^2}{r_{\mathrm{i}}^2-r_{\mathrm{f}}^2}\ln\left(\frac{r_{\mathrm{i}}}{r_{\mathrm{f}}}\right)-1\right]\left[\frac{2r_{\mathrm{c}}^2}{r_{\mathrm{c}}^2-r_{\mathrm{i}}^2}\ln\left(\frac{r_{\mathrm{c}}}{r_{\mathrm{i}}}\right)-1\right]} \tag{A9}$$

$$A_6=\frac{\frac{2r_{\mathrm{c}}^4}{r_{\mathrm{f}}^2\left(r_{\mathrm{c}}^2-r_{\mathrm{i}}^2\right)}\ln\left(\frac{r_{\mathrm{c}}}{r_{\mathrm{i}}}\right)-\frac{3r_{\mathrm{c}}^2-r_{\mathrm{i}}^2}{2r_{\mathrm{f}}^2}}{\frac{2r_{\mathrm{c}}^2}{r_{\mathrm{c}}^2-r_{\mathrm{i}}^2}\ln\left(\frac{r_{\mathrm{c}}}{r_{\mathrm{i}}}\right)-1} \tag{A10}$$

$$\begin{aligned}X_1={}&\left(\frac{r_{\mathrm{i}}^2-r_{\mathrm{f}}^2}{r_{\mathrm{f}}^2}\right)\left[\frac{S_{12}}{2A_1A_3}-\frac{\nu_z^{\mathrm{f}}S_{13}-S_{14}}{8G_{44}^{\mathrm{f}}}\right]+\left[A_4-\frac{A_2A_5}{A_1A_3}\right]\\&\times\left[-\frac{\nu_z^{\mathrm{f}}(S_{23}-S_{13})-(S_{24}-S_{14})}{8G_{44}^{\mathrm{f}}}+\frac{S_{22}-S_{12}}{2A_1A_3}\right]-\frac{A_5}{A_1A_3}\end{aligned} \tag{A11}$$

$$\begin{aligned}X_2={}&1+\left(\frac{r_{\mathrm{i}}^2-r_{\mathrm{f}}^2}{r_{\mathrm{f}}^2}\right)\left[\frac{\nu_z^{\mathrm{f}}S_{13}-S_{14}}{E_z^{\mathrm{f}}}-\frac{S_{11}}{A_5+A_6}\right]\\&+\left[A_4-\frac{A_2A_5}{A_1A_3}\right]\left[\frac{\nu_z^{\mathrm{f}}(S_{23}-S_{13})-(S_{24}-S_{14})}{E_z^{\mathrm{f}}}-\frac{S_{21}-S_{11}}{A_5+A_6}\right]\\&-\frac{1}{A_1}-\frac{A_2}{A_1}\left[-\frac{\nu_z^{\mathrm{f}}(S_{23}-S_{13})-(S_{24}-S_{14})}{8G_{44}^{\mathrm{f}}}+\frac{S_{22}-S_{12}}{2A_1A_3}\right]\end{aligned} \tag{A12}$$

$$X_3=-\frac{A_2}{A_1}\left[\frac{\nu_z^{\mathrm{f}}(S_{23}-S_{13})-(S_{24}-S_{14})}{E_z^{\mathrm{f}}}-\frac{S_{21}-S_{11}}{A_5+A_6}\right] \tag{A13}$$

$$\mathbf{S}=\begin{bmatrix}S_{11}&S_{12}&S_{13}&S_{14}&S_{15}&S_{16}\\S_{21}&S_{22}&S_{23}&S_{24}&S_{25}&S_{26}\\S_{31}&S_{32}&S_{33}&S_{34}&S_{35}&S_{36}\\S_{41}&S_{42}&S_{43}&S_{44}&S_{45}&S_{46}\\S_{51}&S_{52}&S_{53}&S_{54}&S_{55}&S_{56}\\S_{61}&S_{62}&S_{63}&S_{64}&S_{65}&S_{66}\end{bmatrix}=\mathbf{T}^{-1} \tag{A14}$$

$$\mathbf{T}=\begin{bmatrix}\frac{r_{\mathrm{i}}^2-(1+A_4)r_{\mathrm{f}}^2}{r_{\mathrm{f}}^2(A_5+A_6)}&\frac{A_4}{A_5+A_6}&\frac{r_{\mathrm{c}}^2-r_{\mathrm{i}}^2}{r_{\mathrm{f}}^2(A_5+A_6)}-1&1&0&0\\\frac{A_2}{A_1A_3}&-\frac{A_2}{A_1A_3}&1&-1&0&0\\\frac{\nu_z^{\mathrm{i}}}{E_z^{\mathrm{i}}}&0&0&0&\frac{1-\nu_r^{\mathrm{f}}}{E_r^{\mathrm{f}}}+\frac{1}{E_r^{\mathrm{i}}}\left(\frac{r_{\mathrm{i}}^2+r_{\mathrm{f}}^2}{r_{\mathrm{i}}^2-r_{\mathrm{f}}^2}+\nu_r^{\mathrm{i}}\right)&-\frac{2r_{\mathrm{i}}^2}{E_r^{\mathrm{i}}\left(r_{\mathrm{i}}^2-r_{\mathrm{f}}^2\right)}\\-\frac{1}{E_z^{\mathrm{i}}}&0&0&0&-\frac{2\nu_z^{\mathrm{f}}}{E_r^{\mathrm{f}}}-\frac{2r_{\mathrm{f}}^2\nu_z^{\mathrm{i}}}{E_z^{\mathrm{i}}\left(r_{\mathrm{i}}^2-r_{\mathrm{f}}^2\right)}&\frac{2r_{\mathrm{i}}^2\nu_z^{\mathrm{i}}}{E_z^{\mathrm{i}}\left(r_{\mathrm{i}}^2-r_{\mathrm{f}}^2\right)}\\0&-\frac{\nu_z^{\mathrm{i}}}{E_z^{\mathrm{i}}}&\frac{\nu_z^{\mathrm{c}}}{E_z^{\mathrm{c}}}&0&-\frac{2r_{\mathrm{f}}^2}{E_r^{\mathrm{i}}\left(r_{\mathrm{i}}^2-r_{\mathrm{f}}^2\right)}&\frac{1}{E_r^{\mathrm{i}}}\left(\frac{r_{\mathrm{i}}^2+r_{\mathrm{f}}^2}{r_{\mathrm{i}}^2-r_{\mathrm{f}}^2}-\nu_r^{\mathrm{i}}\right)+\frac{1}{E_r^{\mathrm{c}}}\left(\frac{r_{\mathrm{c}}^2+r_{\mathrm{i}}^2}{r_{\mathrm{c}}^2-r_{\mathrm{i}}^2}+\nu_r^{\mathrm{c}}\right)\\0&\frac{1}{E_z^{\mathrm{i}}}&-\frac{1}{E_z^{\mathrm{c}}}&0&-\frac{2r_{\mathrm{f}}^2\nu_z^{\mathrm{i}}}{E_z^{\mathrm{i}}\left(r_{\mathrm{i}}^2-r_{\mathrm{f}}^2\right)}&\frac{2r_{\mathrm{i}}^2\nu_z^{\mathrm{i}}}{E_z^{\mathrm{i}}\left(r_{\mathrm{i}}^2-r_{\mathrm{f}}^2\right)}+\frac{2r_{\mathrm{i}}^2\nu_z^{\mathrm{c}}}{E_z^{\mathrm{c}}\left(r_{\mathrm{c}}^2-r_{\mathrm{i}}^2\right)}\end{bmatrix} \tag{A15}$$

References

[1] Y. Katoh, L.L. Snead, C.H. Henager Jr., A. Hasegawa, A. Kohyama, B. Riccardi, H. Hegeman, J. Nucl. Mater. 367–370 (2007) 659.
[2] R.J. Price, Nucl. Technol. 35 (1977) 320.
[3] R.J. Price, G.R. Hopkins, J. Nucl. Mater. 108&109 (1982) 732.
[4] L.L. Snead, T. Nozawa, Y. Katoh, T.S. Byun, S. Kondo, D.A. Petti, J. Nucl. Mater. 371 (2007) 329.
[5] G.W. Hollenberg, C.H. Henager Jr., G.E. Youngblood, D.J. Trimble, S.A. Simonson, G.A. Newsome, E. Lewis, J. Nucl. Mater. 219 (1995) 70.
[6] L.L. Snead, D. Steiner, S.J. Zinkle, J. Nucl. Mater. 191–194 (1992) 566.
[7] T. Hinoki, Y. Katoh, A. Kohyama, Mater. Trans. 43 (2002) 617.
[8] L.L. Snead, Y. Katoh, A. Kohyama, J.L. Bailey, N.L. Vaughn, R.A. Lowden, J. Nucl. Mater. 283–287 (2000) 551.
[9] T. Hinoki, L.L. Snead, Y. Katoh, A. Hasegawa, T. Nozawa, A. Kohyama, J. Nucl. Mater. 307–311 (2002) 1157.
[10] T. Nozawa, T. Hinoki, L.L. Snead, Y. Katoh, A. Kohyama, J. Nucl. Mater. 329–333 (2004) 544.
[11] T. Hinoki, L.L. Snead, Y. Katoh, A. Kohyama, R. Shinavski, J. Nucl. Mater. 283–287 (2000) 376.

[12] T. Nozawa, K. Ozawa, S. Kondo, T. Hinoki, Y. Katoh, L.L. Snead, A. Kohyama, ASTM STP 1475 (2006) 392.
[13] T. Nozawa, Y. Katoh, L.L. Snead, J. Nucl. Mater. 367–370 (2007) 685.
[14] K. Ozawa, T. Hinoki, T. Nozawa, Y. Katoh, Y. Maki, S. Kondo, S. Ikeda, A. Kohyama, Mater. Trans. 47 (2005) 207.
[15] R.J. Price, Nucl. Technol. 16 (1972) 536.
[16] L.L. Snead, A.M. Williams, A.L. Qualls, ASTM STP 1447 (2003) 623.
[17] T. Nozawa, Y. Katoh, A. Kohyama, Mater. Trans. 46 (2005) 543.
[18] E. Lara-Curzio, M.K. Ferber, J. Mater. Sci. 29 (1994) 6152.
[19] P. Lawrence, J. Mater. Sci. 7 (1972) 1.
[20] R.J. Kerans, T.A. Parthasarathy, J. Am. Ceram. Soc. 74 (1991) 1585.
[21] C.-H. Hsueh, Mater. Sci. Eng. A 154 (1992) 125.
[22] C.-H. Hsueh, Mater. Sci. Eng. A 165 (1993) 189.
[23] C. Liang, J.W. Hutchinson, Mech. Mater. 14 (1993) 207.
[24] D.K. Shetty, J. Am. Ceram. Soc. 71 (1988) C107.
[25] T. Nozawa, L.L. Snead, Y. Katoh, J.H. Miller, J. Nucl. Mater. 371 (2007) 304.
[26] CEGA, Report CEGA-002820, Rev 1 (July 1993).
[27] R.H. Jones, NERI Final Report DE-FG03-990281 (September 2002).
[28] J.L. Kaae, J. Nucl. Mater. 29 (1969) 249.
[29] J.L. Kaae, J. Nucl. Mater. 32 (1969) 322.
[30] J.L. Kaae, J. Nucl. Mater. 46 (1973) 121.
[31] R.J. Price, J.C. Bokros, J. Nucl. Mater. 21 (1967) 158.
[32] J.L. Kaae, Carbon 9 (1971) 291.
[33] R.J. Price, J.L. Kaae, Carbon 7 (1969) 706.
[34] R.J. Price, J.C. Bokros, K. Koyama, Carbon 5 (1967) 423.
[35] Yu.S. Virgil'ev, I.G. Lebedev, Inorg. Mater. 38 (2002) 668.
[36] Product Sheet from Rohm and Haas Company Advanced Materials, Woburn, MA.
[37] B.O. Yavuz, R.E. Tressler, Ceram. Int. 8 (1992) 19.
[38] Product Sheet from Nippon Carbon Co. Ltd., Japan.
[39] J.Y. Yan, C.W. Chen, P.C. Fang, K.M. Yin, F.R. Chen, Y. Katoh, A. Kohyama, J.J. Kai, J. Nucl. Mater. 329–333 (2004) 513.
[40] J. Tersoff, Phys. Rev. B 39 (1989) 5566.
[41] B. Northey, D. Peters, T. Nozawa, Y. Katoh, L.L. Snead (unpublished work).
[42] Z. Hashin, J. Appl. Mech. 46 (1979) 543.
[43] Y. Katoh, L.L. Snead, T. Hinoki, S. Kondo, A. Kohyama, J. Nucl. Mater. 367–370 (2007) 758.
[44] S. Kondo, A. Kohyama, T. Hinoki, J. Nucl. Mater. 367–370 (2007) 764.
[45] Y. Mikata, M. Taya, J. Compos. Mater. 19 (1985) 554.
[46] J.-L. Bobet, J. Lamon, Acta Metall. Mater. 43 (1995) 2241.
[47] H.J. Oel, V.D. Frechette, J. Am. Ceram. Soc. 69 (1986) 342.
[48] E. Vagaggini, J.-M. Domergue, A.G. Evans, J. Am. Ceram. Soc. 78 (1995) 2709.
[49] C.H. Henager Jr., E.A. Le, R.H. Jones, J. Nucl. Mater. 329–333 (2004) 502.
[50] W. Yang, A. Kohyama, T. Noda, Y. Katoh, T. Hinoki, H. Araki, J. Yu, J. Nucl. Mater. 307–311 (2002) 1088.
[51] T. Hinoki, W. Yang, T. Nozawa, T. Shibayama, Y. Katoh, A. Kohyama, J. Nucl. Mater. 289 (2001) 23.
[52] S. Kondo, Y. Katoh, L.L. Snead, Neutron irradiation-induced void and dislocation structures in SiC, in: 13th International Conference of Fusion Reactor Materials, Nice, France, 2007.
[53] B. Budiansky, J.W. Hutchunson, A.G. Evans, J. Mech. Phys. Solids 34 (1986) 167.
[54] K.H. Park, S. Kondo, Y. Katoh, A. Kohyama, Fus. Sci. Technol. 44 (2003) 455.
[55] Y. Katoh, T. Nozawa, L.L. Snead, T. Hinoki, J. Nucl. Mater. 367–370 (2007) 774.
[56] W.A. Curtin, J. Am. Ceram. Soc. 74 (1991) 2837.